

Dynamics and Energetics of the Mammalian Phosphatidylinositol Transfer Protein Phospholipid Exchange Cycle

Aby Grabon^{1†}, Adam Orłowski^{2,3†}, Ashutosh Tripathi¹, Joni Vuorio², Matti Javanainen², Tomasz Róg^{2,4}, Max Lönnfors¹, Mark I. McDermott¹, Garland Siebert¹, Pentti Somerharju⁵, Ilpo Vattulainen^{2,4,6*}, and Vytas A. Bankaitis^{1,7,8*}

¹Department of Molecular and Cellular Medicine, Texas A&M Health Science Center
College Station, Texas 77843-1114 U.S.A.

²Department of Physics, Tampere University of Technology Korkeakoulunkatu 10, FI-33720 Tampere, Finland

³Department of Physics and Energy, University of Limerick, Limerick, Ireland

⁴Department of Physics, University of Helsinki, P.O. Box 64FI-00014 Helsinki, Finland

⁵Faculty of Medicine, Department of Biochemistry and Developmental Biology
University of Helsinki, Helsinki, Finland

⁶Department of Physics and Chemistry, MEMPHYS – Center for Biomembrane Physics
University of Southern Denmark, Campusvej 55, DK-5230 Odense, Denmark

⁷Department of Biochemistry and Biophysics, Texas A&M University
College Station, Texas 77843 U.S.A.

⁸Department of Chemistry, Texas A&M University
College Station, Texas 77843 U.S.A.

Running title: Anatomy of the PITP lipid exchange cycle

Key words: PITP, lipids, phosphoinositide signaling, molecular dynamics simulations

† These authors contributed equally to the work.

* Co-Corresponding authors: ilpo.vattulainen@tut.fi; vytas@tamhsc.edu

ABSTRACT

Phosphatidylinositol-transfer proteins (PITPs) regulate phosphoinositide signaling in eukaryotic cells. The defining feature of PITPs is their ability to exchange phosphatidylinositol (PtdIns) molecules between membranes, and this property is central to PITP-mediated regulation of lipid signaling. Yet, the details of the PITP-mediated lipid exchange cycle remain entirely obscure. Here, all-atom molecular dynamics (MD) simulations of the mammalian StART-like PtdIns/ phosphatidylcholine (PtdCho) transfer protein PITP α , both on membrane bilayers and in solvated systems, informed downstream biochemical analyses that tested key aspects of the hypotheses generated by the MD simulations. These studies provided five key insights into the PITP α lipid exchange cycle: (1) interaction of PITP α with the membrane is spontaneous and mediated by four specific protein substructures, (2) the ability of PITP α to initiate closure around the phospholipid ligand is accompanied by loss of flexibility of two helix/loop regions as well as of the C-terminal helix, (3) the energy barrier of phospholipid extraction from the membrane is lowered by a network of hydrogen bonds between the lipid molecule and PITP α , (4) the trajectory of PtdIns or PtdCho into and through the lipid-binding pocket is chaperoned by sets of PITP α residues conserved throughout the StART-like PITP family, and (5) conformational transitions in the C-terminal helix have specific functional involvements in PtdIns transfer activity. Taken together, these findings provide the first mechanistic description of key aspects of the PITP α PtdIns/PtdCho exchange cycle, and offer a rationale for the high conservation of particular sets of residues across evolutionarily distant members of the metazoan StART-like PITP family.

INTRODUCTION

Phosphatidylinositol (PtdIns) is a metabolic precursor of phosphoinositides, and these lipids function as critical intracellular chemical signals in eukaryotes. While much effort is invested in understanding the enzymes that produce and consume phosphoinositides, fundamental aspects for how phosphoinositide production is regulated and physically organized define unappreciated gaps in our understanding of how inositol lipid

signaling is prosecuted in cells. It is in those contexts that PtdIns transfer proteins (PITPs) command increasing interest as activities that functionally channel lipid metabolic information to dedicated and tightly integrated phosphoinositide signaling circuits. It is therefore no surprise that the biological importance of PITPs is on striking display in both uni- and multi-cellular organisms. Phenotypes associated with defects in individual PITPs include: (i) non-redundant functions of individual PITPs in channeling phosphoinositide signaling to Golgi/endosomal membrane trafficking, lipid droplet metabolism, and endosomal phosphatidylserine metabolism in yeast [1-4], (ii) collapse of 'extreme' polarized plant membrane growth programs required for tissue organogenesis [5-7], (iii) defects in embryogenesis and retinal degeneration disease in both *Drosophila* and zebrafish [8-11], and (iv) neurodegeneration, chylomicron retention disease, liver steatosis, and hypoglycemia in neonatal mice [12-14].

The biological importance of these proteins notwithstanding, PITPs remain poorly characterized with respect to how these proteins work as molecules. PITPs are not enzymes, but proteins that mobilize energy-independent transfer of PtdIns and PtdCho between membranes *in vitro* [15,16]. On the basis of this operational assay, PITPs have historically been described to function as lipid carriers that transport PtdIns from its site of synthesis in the endoplasmic reticulum to the plasma membrane where agonist-stimulated phospholipase C-dependent pathways consume phosphoinositides -- for which PtdIns is a metabolic precursor [16]. An alternative mechanistic framework for thinking about how PITPs function as molecules is gaining strong momentum, however, and it conceptualizes a very different mechanism which does not involve inter-membrane PtdIns-transfer at all. Rather, PITPs are proposed to chaperone tightly channeled synthesis of privileged phosphoinositide pools dedicated to specific biological outcomes [17-19].

Regardless of whether PITPs function as PtdIns presentation modules, or as bona fide PL-transfer proteins, there is no question that the PL-exchange reaction is central to their biological activity. The broad outline of the exchange reaction can be conceptualized by the PITP

ejecting bound PL upon docking onto a membrane surface, followed by reloading of the PITP with another PL molecule prior to its disengagement from the surface. Studies in purified systems with defined liposomes and purified recombinant PITP demonstrate that abstraction of PL from a stable membrane bilayer during the exchange reaction occurs in the absence of any other co-factors or ATP [15,16]. Thus, PITPs somehow lower the activation energy of PL desorption from the bilayer – presumably by coupling protein conformational transitions to a cycle of PL unloading and loading. However, the fundamental details of the protein and PL dynamics associated with the exchange reaction are proving exceptionally challenging to dissect using conventional wet biochemistry approaches alone.

The first atomistic insights into the conformational dynamics associated with PL-exchange were obtained from unrestrained MD simulations and biochemical analyses of the major yeast PITP Sec14 [20]. Although the MD time course was short (32 ns), oscillations between ‘open’ and ‘closed’ Sec14p conformers were simulated and Sec14 structural elements were identified that control the conformational dynamics pathway associated with such oscillations. These included a flexible helical substructure that gates access to the PL binding pocket, a hinge region that supports helical gate motions, and a conformational switch element (the G-module) that couples gate dynamics with membrane/PL binding [20,21]. The Sec14 conformational circuitry described by those simulations is likely to be broadly conserved across the Sec14 protein superfamily, and available evidence makes the case that defects in this circuitry underlie inherited disease-associated mutations in mammalian Sec14-like proteins [20].

While informative, those Sec14 simulations are limited. First, the MD simulations were conducted in the absence of a membrane bilayer. Thus, no information was forthcoming regarding PL::PITP interactions during the exchange reaction [20]. Fundamentally, it is those interactions that must be understood. Second, the detailed information gleaned from the Sec14 MD simulations does not translate to the vertebrate StART-domain PITPs given that the two classes of PITPs are structurally unrelated. This issue takes

on added force given the dramatic developmental and neurodegenerative phenotypes associated with genetic deficiencies in StART-domain PITP function in vertebrates and other metazoans [8-13]. As first address of these major gaps in our knowledge, we describe herein the protein and PL dynamics, and the free energy landscape, of PtdIns and PtdCho exchange by the mammalian StART-domain PITP α .

RESULTS

PITP α binding to the membrane bilayer. Both open apo-PITP α and closed PtdCho-bound holo-PITP α forms have been crystallized and high-resolution structures solved [22,23]. The protein consists of four domains. The PL-binding cavity includes: (i) an 8-stranded β -sheet capped by two long α -helices, (ii) a regulatory loop speculated to be involved in mediating protein interactions, (iii) the C-terminal domain suggested to participate in closure of the PL-binding pocket, and (iv) a small lipid exchange loop speculated to form a lid over the PL binding pocket and thereby gate access to it (Figure 1A).

To examine the PITP α lipid exchange cycle at an atomistic level, extensive all-atom MD of both the open and closed PITP α conformers were run in systems reconstituted with bilayers consisting of PtdCho or PtdIns/PtdCho (Supplementary Table S1). RMSD and RMSF plots of PITP α C α -atoms showed that both conformers were stable during the simulations (Figure 1B and C). Higher flexibility was observed for the open conformer in the presence of the PtdCho/PtdIns membrane (Figure 1B, lower right panel), and this was primarily accounted for by the increased flexibility of the PITP α extreme C-terminus (Figure 1C – lower right panel). That is, the substructure suggested to gate access to the PITP α hydrophobic pocket.

The substructure bounded by residues 25-38 similarly exhibited enhanced flexibilities in the open conformer relative to the closed holo-PITP α . Indeed, it is in that former substructure that the most striking conformational change was observed during the MD. In all simulations involving the open PITP α conformer, the lipid exchange loop (bounded by residues 65-83) also transitioned from a turn in the starting structure into a 3₁₀-

helical conformation during the MD simulation as evaluated by the Define Secondary Structure of Proteins (DSSP) algorithm that uses H-bond networks to classify secondary structure [24]. In one simulation (system 4, open PITP α conformer), that conformational change coincided with insertion of the lipid-exchange loop into the bilayer upon PITP α association with the membrane.

To further characterize the stable and firm binding of PITP α to membrane we used both theoretical and experimental data to define two criteria for identifying the most likely ‘on pathway’ trajectories. First, trajectories that reported binding of the Trp₂₀₃Trp₂₀₄ motif to the membrane surface were considered to be ‘on pathway’ given experimental evidence suggesting those residues to be important for membrane binding and lipid exchange by StART-like PITPs [25-27]. Second, trajectories that were consistent with theoretical predictions from the Orientation of Proteins in Membranes (OPM) database [28]; using pdb files for ‘open’ and ‘closed’ PITP α structures

[<http://opm.phar.umich.edu/protein.php?pdbid=1kcm>] and

[<http://opm.phar.umich.edu/protein.php?pdbid=1uw5>, respectively] were also considered to be ‘on pathway’.

Based on these criteria, we observed a firm and spontaneous PITP α binding to membrane in the following simulations: PtdCho/PtdIns membrane with closed PITP α repeats 1 and 2, PtdCho membrane with closed PITP α repeats 1 and 2, PtdCho/PtdIns membrane with open PITP α repeats 1 and 3, PtdCho membrane with open PITP α repeats 1 and 3. Our discussion on the results and presentation of averaged data is based on these systems unless otherwise stated.

Rationale for this choice can be viewed in Supplementary Movies S1-S12 where the residues Trp₂₀₃ and Trp₂₀₄ are depicted and were observed to undergo association with membrane. Moreover, the pattern of binding scored by the number of H-bonds established between protein and PL (Supplementary Figure S1A) was consistent within these systems. Initial (0 ns) and final (1 μ s) snapshots for all four representative simulations are presented in Figure 2, and the time evolution

of each membrane association event is documented in Supplementary Movies S1-S12.

Detailed analyses of the occurrence of H-bond interactions between individual PITP α residues and PLs are compiled in Supplementary Tables S2 and S3. Although the residues identified for membrane binding differed between the open and closed conformers in the PtdCho-only systems, some residues were consistently highlighted and those identified three common regions involved in membrane association. Those regions were defined by: (i) the lipid exchange loop (residues 68-81), (ii) residues 135-163, and (iii) residues 204-220. With regard to specific interactions, Tyr₁₀₃ of the open conformer engaged the PtdIns/PtdCho membrane in hydrogen bond interactions, whereas the C-terminal lid domain of the closed conformer (residues 259-264) interacted specifically with the PtdCho-only membrane. Parallel analyses in the PtdIns/PtdCho systems identified residues 147-153 and 208-219 in PITP α ::PtdIns interactions (Supplementary Table S3).

Occurrence of contacts between PITP α and PL atoms were similarly monitored throughout the MD course where contact was set as an inter-atomic distance of ≤ 0.35 nm (Supplementary Figure S1B). Those analyses indicated that, in addition to the regions identified by H-bond analyses, both conformers showed residues 28-41 constituted another region of membrane association region we term MAR1. Moreover, the open conformer uniquely presented one additional membrane association region we term MAR2 (residues 99-110), and this particular set involved interactions other than H-bonds (e.g. charge pairs). This unique membrane association area was able to interact with the bilayer surface due to the slightly different dock orientation of the open PITP α conformer on the membrane surface relative to that of the closed form -- a difference which renders this protein region more accessible to the membrane for binding. For purposes of clarity, these MAR1 and MAR2 motifs are identified on the PITP α structure in Figure 1A.

PITP α dynamics upon membrane association.

After membrane binding, the closed PITP α molecule remained relatively inert throughout the

remainder of the simulation. No unloading of bound PtdCho or opening of the lid was observed (Supplementary Movies 1-6). Specific conformational motions were observed upon membrane binding for the open PITP α conformer, however, and it is for this reason that focus was trained on this conformer. Interestingly, residues 25-38, implicated in membrane binding, exhibited enhanced mobility in the open form. Moreover, using the inter-atomic distance between residues Ser₃₀ and Glu₄₁ as ruler for pocket closure, that distance decreased dramatically until it approached that observed in the closed conformer (Figure 3, Supplementary Figure S2).

The lipid exchange loop was also inserted into the cytoplasmic leaflet of the bilayer at this time where it underwent a transition from a turn to a 3₁₀-helix as indicated by DSSP analysis, and adopted a more extended conformation as reported by RMSF calculations (Figure 1C) and by visual inspection (Figure 3A,B). Most interestingly, bilayer insertion of the lipid exchange loop (and the partial closure of the hydrophobic pocket) coincided with partial loading of a single PtdCho molecule into the open pocket (Figure 3C,D). We interpret the simulation data to conceptualize engagement of the lipid exchange loop with one PtdCho molecule with the result that the engaged PtdCho was extracted from the membrane bilayer and moved towards the hydrophobic pocket/water interface. PITP α was unable to consolidate those movements into vectorial transfer of PL into the hydrophobic pocket, however. Rather, the partially extracted PLs either slid back into the bilayer or engaged in bobbing movements at the cavity opening/water interface.

The role of PITP α residues Trp₂₀₃ and Trp₂₀₄ in the lipid exchange cycle is unclear. Several studies conclude those residues are essential for lipid exchange by PITP α and closely-related PITPs [25,26], whereas other studies argue for minor roles for Trp₂₀₃Trp₂₀₄ in lipid-exchange [27]. Nonetheless, Trp₂₀₃Trp₂₀₄ were the first residues to interact with the lipid bilayer, and the Trp₂₀₃Trp₂₀₄ motif maintained interactions with membrane lipids throughout the MD time course. The MD suggest those Trp residues, and the residues that surround them, interact primarily with PtdIns (Supplementary Figure S1B).

Functional analyses of Ser₂₅ in PITP α activity.

Residues 25-38 define a flexible region predicted to be involved in membrane binding, and the boundary residue Ser₂₅ is projected to be involved in H-bonding to PtdCho and PtdIns within the PITP α hydrophobic pocket. To assess the importance of Ser₂₅ to PITP α function, this residue was altered to Phe, Ala, Cys, Glu, Lys, and Thr. All mutant proteins were confirmed to be stable when expressed in yeast (Supplementary Figure S3). Mutant proteins were subsequently analyzed in *in vivo* and *in vitro* functional assays.

High-level expression of PITP α in yeast is sufficient to effect phenotypic rescue of the growth and membrane trafficking defects associated with temperature-sensitive mutations in the yeast *SEC14* gene [29], and this system enabled a general assessment of whether a mutant PITP α is functional or not. Expression of PITP α ^{S25A}, PITP α ^{S25C} and PITP α ^{S25T} rescued *sec14-1^{ts}*-associated growth defects at the restrictive temperature of 37°C at an efficiency similar to that observed for PITP α (Figure 4A). By contrast, PITP α ^{S25E} was only partially functional in this assay whereas PITP α ^{S25F} and PITP α ^{S25K} scored as completely defective. Consistent with the *in vivo* results, purified recombinant PITP α ^{S25F} and PITP α ^{S25K} were also completely inactive for PtdIns and PtdCho-transfer *in vitro* in end-point assays using radiolabeled phospholipid substrates and a single clamped protein concentration (Figure 4B). Thus, while some substitutions were tolerated for Ser₂₅, the functionality pattern did not correlate with H-bonding capacity (e.g. S₂₅A scored as active). Rather, activity correlated best with the accessible surface area of the residue at that position. Residues compatible with efficient function (Ser, Ala, Cys, Thr) have small accessible surface areas (80Å², 67Å², 104Å², 102Å², respectively), those that supported partial function have larger values (Glu, 138Å²), and residues not tolerated had the largest side chains (Phe, Lys; accessible surface areas of 175Å² and 167Å², respectively).

Real-time de-quenching approaches were used as independent assays to separately monitor PtdCho- and PtdIns-transfer rates. In those assays, transfer was recorded as enhanced fluorescence of pyrene-labeled phospholipid as it was mobilized from quencher-loaded donor vesicles to quencher-

free acceptor vesicles (see Materials and Methods). The significantly reduced initial rates of PtdCho- and PtdIns-transfer by PITP α ^{S25E} and PITP α ^{S25K} were recapitulated in those experimental systems (Figure 4C). These assays were able to resolve a small amount of PtdIns-transfer capacity for PITP α ^{S25E}, which accounts for the mutant's modest ability to rescue Sec14 deficiency *in vivo* (Figure 4A,C).

Free energies of PL loading/unloading by PITP α . The 1000 ns atomistic MD runs were of insufficient length to describe a complete PL loading/unloading half-cycle. Thus, suitable free-energy calculation methods were employed to study the energetics of PL loading/unloading by PITP α . A steered MD simulation approach was used to obtain a pathway for positioning of PtdCho and PtdIns within the PITP α binding pocket through a short pulling simulation (see Materials and Methods). Once this regime yielded a PL-loaded conformer, the pulling constraints imposed on PL position were released, and subsequent trajectories were used to extract the windows for umbrella sampling simulations. Those umbrella sampling simulations were then analyzed with WHAM (see Materials and Methods). Our selection of the force constant, together with the window spacing, provided sufficient sampling of the configuration space along the reaction coordinate as indicated by the satisfactory overlap of the histograms in Supplementary Figure S4A. Moreover, although each window was simulated for 40 ns, the obtained PMF stabilized within 10 ns of simulation – indicating the free energy profile converged to a stable value. We interpret this rapid convergence to reflect the fact that the starting structures for the umbrella sampling windows were extracted from unbiased trajectories. This interpretation follows previous demonstrations that the qualities of the starting structures for umbrella sampling have a significant impact on subsequent free energy profile quality [30].

Because the exchange cycle occurs efficiently with purified PITP α and pure liposomes, and without any ATP requirement, the activation energy for PL loading/unloading must be sufficiently low to be overcome by thermal fluctuations. Indeed, during the ensuing MD

simulations (150 and 240 ns for the systems with PtdCho and PtdIns, respectively), bound PL was unloaded from the binding pocket and released into the bilayer (Figure 5A). The PL unloading took place without any externally applied pulling forces. Taking advantage of these well-equilibrated starting configurations, umbrella sampling simulations were extracted from the unloading trajectories and the free energies related to PITP α interaction with PtdCho and PtdIns were calculated. The free energy profiles for both PLs as a function of the distance along the bilayer normal are presented in Figure 5B. Those profiles confirmed that PL loading into PITP α occurs within the realm of thermal fluctuation. The free energy of PtdCho uptake by PITP α was ~ 20 kJ mol⁻¹ (8 k_BT) -- as calculated from the bottom of the global minimum to the maximum peak at 3 nm (Figure 5B). The values for PtdCho and PtdIns desorption from the membrane bilayer were 90 kJ mol⁻¹ and 120 kJ mol⁻¹, respectively (Supplementary Table S4). The dramatic differences in the free energies of PL desorption in the presence vs. absence of PITP α emphasize the remarkable role the protein plays in lowering the activation energy for that critical step.

For both PtdCho and PtdIns, the free energy profiles identified two distinct minima. The first, at 1.5 nm, corresponded to the state where the PL was at equilibrium in the bilayer. The second was located in the membrane-distal region of the PL-binding cavity where the PL headgroups are coordinated by appropriate PITP α residues and the fatty acyl chains are incorporated into the most hydrophobic regions of the cavity. Unexpectedly, the free energies of loading for both PLs were similar – suggesting the affinity of PITP α for PtdIns in the initial loading stage(s) was not appreciably higher than that for PtdCho. This was an unexpected outcome given crude estimates that PITP α has a 16-fold higher affinity for PtdIns than for PtdCho [15,16]. Another remarkable feature of the calculated free energy profiles was that the minima at ~ 3.5 nm were very shallow. This property neatly accounts for why PL molecules that had partially loaded, or were otherwise steered, into the PITP α pocket were spontaneously and efficiently released into the bilayer via a reverse unloading reaction during simulation. That

is, the energy barrier for unloading of bound PL is low.

PITP α -PL interactions within the hydrophobic pocket. Lipid-protein H-bond interactions within the PITP α hydrophobic pocket are likely required for serial consolidation of the loading reaction so that vectoriality is imposed on this process, which culminates in a complete loading reaction (i.e. rather than the reversible and futile partial loading reaction observed in the 1000 ns MD). Indeed, both PtdCho and PtdIns engaged in H-bonding within the PITP α binding pocket, and the highest peaks in average H-bond interaction coincided with minima in the free energy profiles (Figure 5B and C). Those results argued that H-bond interactions make critical contributions to the free energy landscapes of the PtdCho and PtdIns loading/unloading reactions.

All pocket residues involved in H-bonding with PtdCho and PtdIns are highlighted in Figure 5C. The unloading MD runs forecast that Lys₆₈ interacted primarily with PtdCho, whereas Thr₅₉, Lys₆₁, Glu₈₆, Asn₉₀, Thr₁₁₄, and Glu₂₁₈ interacted primarily with PtdIns. Satisfyingly, the former four residues were known from previous studies to engage PtdIns specifically [25,31], while the latter two interactions represent new insights. Tyr₁₈, Gln₂₂, Ser₂₅, Tyr₆₃, Asn₁₀₁, Lys₁₉₅, and Gln₂₁₇ formed H-bonds with both PtdCho and PtdIns, and those residues had not previously been recognized to play any role in the PL-exchange cycle. The strong single H-bond interaction of Lys₆₈ with PtdCho was particularly noteworthy as it was observed early in the loading reaction sequence (Supplementary Figure S4B) – suggesting this previously unsuspected interaction plays a role in the PtdCho extraction process. PtdIns did not interact strongly with PITP α residue Lys₆₈. Rather, it formed two H-bonds with Glu₂₁₈ -- another residue previously not suspected to play any role in lipid exchange (Supplementary Figure S4B). The MD projected that interactions of PtdCho and PtdIns with Lys₆₈ and Glu₂₁₈, respectively, defined the major contribution to peaks in the average H-bond plot at ~2.3 nm (Figure 5C).

Functional analyses of Glu₂₁₈ and Lys₆₈ in PL-transfer and binding. Lys₆₈ is a candidate residue for engaging PtdCho early in the PITP α loading

reaction. Structure-function experiments demonstrated PITP α ^{K68E} or PITP α ^{K68R} expression was less efficient in phenotypic rescue of *sec14-1^{ts}*-associated growth defects relative to wild-type protein (Figure 6A). Other substitutions were reasonably well-tolerated as evidenced by PITP α ^{K68A}, PITP α ^{K68C} and PITP α ^{K68Q} scoring as functional proteins in that assay. The biochemical properties of purified PITP α ^{K68E} were further examined in the end-point PtdCho and PtdIns transfer assays. Consistent with the predictions of the MDS, PITP α ^{K68E} showed a ~70% reduction in PtdCho-transfer activity (Figure 6B). However, the mutant PITP was also strongly defective in PtdIns-transfer -- even though the MDS did not reveal strong interactions of Lys₆₈ residue with this PL. Real-time de-quenching analyses confirmed the significantly reduced initial rates of PtdCho- and PtdIns-transfer and binding by PITP α ^{K68E} (Figures 6C,D).

Unlike Lys₆₈, residues Thr₁₁₄ and Glu₂₁₈ were scored to interact predominantly with PtdIns. Analyses of Thr₁₁₄ substitution mutants proved fruitless as the mutants were unstable proteins when expressed in yeast and, in all cases, the mutant proteins quantitatively partitioned into inclusion bodies when expressed as recombinant proteins in *E. coli*. Thus, our analyses focused on Glu₂₁₈, and this residue was of interest given that it was projected to form two H-bonds with PtdIns during the MD. Nonetheless, PITP α ^{E218A}, PITP α ^{E218D}, and PITP α ^{E218K} all scored as functional in the phenotypic rescue assay (Figure 7A). Both end-point and real-time PtdIns- and PtdCho-transfer de-quenching assays also showed PITP α ^{E218A} was not significantly compromised for either PtdIns- or PtdCho-transfer activity (Figures 7B,C). However, the mutant protein was compromised for both PtdIns- and PtdCho-binding (Figure 7D).

Functional analyses of Lys₁₉₅ in PtdIns and PtdCho-transfer and binding.

Lys₁₉₅ was highlighted in the MD simulations as a major contributor to the interaction of both PtdIns or PtdCho within the PITP α lipid binding cavity (Figure 8). Moreover, in independent analyses, we serendipitously highlighted this same residue in a Cys-scanning mutagenesis screen on the basis of the 2.3Å and 2.7Å distance between Lys₁₉₅ and the

phosphate moieties of bound PtdIns and PtdCho, respectively (unpublished data). Thus, P1TP α ^{K195C} was purified and analyzed with respect to PtdCho- and PtdIns-transfer rates and efficiencies of PtdCho- and PtdIns-binding (Figure 8A,B, respectively). P1TP α ^{K195C} scored as nonfunctional in the yeast P1TP activity assay as its expression was unable to rescue growth of *sec14^{ts}* yeast mutants at 37°C (Figure 8A). P1TP α ^{K195C} did not transfer PtdIns or PtdCho in the radiolabel transfer assay (Figure 8B) and, as expected, was unable to transfer (Figure 8C) or bind (Figure 8D) pyrene-labeled PtdIns or PtdCho.

Conformational transitions of the P1TP α C-terminal helix contribute to ligand specificity.

PtdIns is the preferred exchange substrate for P1TP α but the 1000ns all-atom simulations of membrane-bound P1TP α were not informative regarding what headgroup-specific conformational transitions of the P1TP might contribute to such ligand specificity. To understand how large conformational changes contribute to the ability of P1TP to bind lipids, P1TP α dynamics were simulated in a solvated system. In those simulations, the conformational transitions of apo-P1TP α , the open PtdIns-bound conformer and the open PtdCho-bound were compared. The latter two starting structures were generated by assigning PtdIns or PtdCho to their respective positions within the hydrophobic pocket as defined by X-ray crystallography (see Methods and Materials). MDS (250ns) revealed conformational transitions from the open to the closed conformation.

Of relevance to this study, we focus on the C-terminal G-helix. Even though G-helix lies on the P1TP α surface, and its side-chains have no direct interaction with either PL (distance > 8Å), this substructure exhibited differential dynamics in the 250 ns MD simulations depending on whether PtdIns or PtdCho was loaded into the open P1TP α conformer. In both the open apo-P1TP α and P1TP α ::PtdCho MDS, the G-helix remained stable and no major uncoiling was observed (helix length avg. 22Å, from Thr₂₄₀ to Asp₂₅₆; Figure 9A). This helix underwent a conspicuous melting in systems modeling the open P1TP α ::PtdIns conformer, however (helix length avg. 15Å, from Thr₂₄₀ to Glu₂₅₀). Of note was a kinking of the helix at

residue Glu₂₄₈ -- an invariant residue amongst the StART-like P1TPs (Figure 9B).

In the open P1TP α ::PtdCho conformer the Glu₂₄₈ side-chain was disposed to solvent on the G-helix surface and pointed away from the PtdCho headgroup. In that orientation, the side-chain was in H-bond contact with G-helix residues Arg₂₄₅ and Lys₂₅₂ (both invariant StART-like P1TP residues) -- thereby stabilizing the helical secondary structure. In the case of P1TP α ::PtdIns, however, Glu₂₄₈ was initially oriented towards the PtdIns headgroup. As the open P1TP α ::PtdIns conformer closed, however, the G-helix distorted and the Glu₂₄₈ side-chain twisted away from the PtdIns headgroup towards the protein surface. In that orientation, Glu₂₄₈ was primarily engaged in electrostatic interaction with Lys₂₅₂. Residue Met₂₄₁ sits at the N-terminal end of the G-helix and it too is invariant amongst the StART-like P1TPs. Interestingly, Met₂₄₁ and Ile₂₄₄ (also highly conserved) engaged Leu₂₃ on the N-terminal A-helix via van der Waals interactions (Figure 9C) -- suggesting an involvement for Met₂₄₁ and Ile₂₄₄ in stabilizing the A-helix. Those results offered a specific hypothesis for why the G-helix showed headgroup-specific dynamics given A-helix residues Tyr₁₈, Gln₂₂ and Ser₂₅ were identified as interacting with PtdIns and PtdCho in the 1000 ns MDS of membrane-bound P1TP α .

Glu₂₄₈ and Met₂₄₁ execute specific functions in PtdIns-transfer and binding. To determine whether the G-helix exhibits consequential headgroup-specific involvements in P1TP α -mediated PL-exchange, the functional properties of Glu₂₄₈ mutants were analyzed in detail. Indeed, missense substitutions at that position levied strong selectivity for PtdIns-transfer and PtdIns-binding relative to PtdCho binding/transfer. In the phenotypic rescue assay, only P1TP α ^{E248D} showed activity while P1TP α ^{E248K}, P1TP α ^{E248A} and P1TP α ^{E248T} all scored as strongly defective (Figure 10A). The defects from the rescue assay were recapitulated in PtdIns-transfer assays -- even though these mutant proteins retained wild-type abilities to transfer/bind PtdCho in end-point assays (Figure 10B). P1TP α ^{E248A} was also analyzed in the de-quenching assay system where it again scored as completely defective for PtdIns-transfer, but showed essentially wild-type PtdCho-transfer

activity (Figure 10C). Those headgroup-selective defects were further confirmed in real-time binding measurements where PIP α ^{E248A} showed no PtdIns-binding activity in the time-course of the assay while remaining fully competent for PtdCho-binding (Figure 10D).

The biochemical consequences of altering Met₂₄₁ were similarly analyzed. This residue was of particular interest not only for structural reasons as bridge between the G- and A-helices, but the M₂₄₁T missense substitution is the consequence of a SNP circulating in the human population [32]. As observed for the PIP α ^{E248A,K,T} mutants, PIP α ^{M241T} was selectively compromised for PtdIns-transfer activity. The mutant protein exhibited a 50% decrease of PtdIns-transfer activity with no diminution in its ability to transfer PtdCho (Figure 10B).

DISCUSSION

The PL-exchange cycles of PIPs are essential to their critical functions in stimulating the activities of PtdIns 4-OH kinases for biologically sufficient production of phosphoinositides [18]. The basic form of this cycle, however, is not at all understood for any PIP. Herein, we describe a series of unrestrained MD simulations of mammalian PIP α that most likely modeled interfacial processes associated with the initial steps of PIP α reloading with PL after ejection of a previously bound PL molecule. Moreover, the simulations supported first calculations of the free energy landscape of PtdIns and PtdCho exchange by mammalian PIP α . Additional simulations of PIP α in membrane-free systems described conformational transitions that modulate the lipid exchange cycle in surprisingly long-range and lipid headgroup-specific ways. These collective studies report new insights into the initial stages of PL-exchange by PIP α , describe H-bonding interactions between PL and protein within the PIP α hydrophobic pocket, and provide the first clues as to how PIPs lower the activation energy of PL desorption from the membrane bilayer.

PIP α binding to membrane surfaces. Both the ‘closed’ and the ‘open’ PIP α conformers spontaneously bound membrane surfaces in equilibrium MD simulations, and the binding events were stable and occurred in the course of

relatively short timescales (~200 ns). Membrane binding consisted of three components. The first were direct interactions of the PIP with lipid at the membrane surface as counted by the number of H-bonds established between protein and PL. This component involved two separate regions bound by residues Lys₁₃₅-Lys₁₆₃ and Trp₂₀₄-Arg₂₂₀ as membrane association domains. The second component was unique to the open PIP α conformer and involved a membrane insertion unit (the lipid exchange loop defined by residues Lys₆₈-Ala₈₁) that penetrated into the bilayer and initialized the first steps of the PL-loading reaction of the PIP α lipid exchange cycle. The third component described PIP α conformational transitions that accompanied membrane binding/insertion events. One of these motions involved lipid exchange loop (Lys₆₈-Ala₈₁) penetration into the bilayer. The other involved increased conformational flexibility and membrane association of residues Ser₂₅-Glu₄₁. The importance of this region to PIP α activity was confirmed by mutational analyses that were consistent with Ser₂₅ playing a key role in the conformational flexibility of this PIP α subdomain, and this flexibility being required for PL-exchange.

Initial steps of PL-loading into apo-PIP α . The MD simulations predicted that a consequence of lipid exchange loop insertion into a mixed bilayer was a partial loading of the open PIP α conformer with a single PtdCho molecule (at 700 ns in the simulation). This partial extraction of PtdCho from bilayer into the PIP α hydrophobic pocket was accompanied by a shielding of the fatty acyl chains from bulk membrane by the lipid exchange loop, and partial closure of the unit that gates accessibility to the lipid binding pocket. Functional assays indicated amino acid substitutions in this substructure (i.e. for Lys₆₈) compromised both PtdCho and PtdIns binding and exchange activities. It is now both a reasonable and attractive proposition that the inserted lipid exchange loop is the first protein substructure to interact with a PL molecule, and that this interaction marks that PL molecule as a PIP α exchange ligand.

The progress in describing initial steps of the PL exchange cycle notwithstanding, we were

unable to simulate full incorporation of PL into the PITP α lipid binding pocket. Rather, the ‘chosen’ PtdCho molecule entered a futile exchange reaction characterized by a shallow breathing conformational dynamics regime and ultimately fell back into the bilayer. Our interpretation is that the partially loaded PL encounters a free energy well at an early step in the exchange cycle, and that this barrier cannot be negotiated during 1000 ns simulation windows used in these experiments. Complete uptake of PL into the PITP α lipid binding pocket requires extending simulation timescales sufficiently to allow additional conformational transitions to occur that direct the ‘open’ PITP α from a shallow breathing regime to one that consolidates the PL-extraction process by supporting trajectories converging onto a closed conformer. An alternative, and not mutually exclusive, possibility is that the compositionally simple bilayers modeled themselves created a significant energy barrier that could not be negotiated during the 1000 ns MD. Natural membranes exhibit packing irregularities that might be productively exploited by the PITP α molecule in initiating a lipid exchange cycle, and such packing irregularities were minimal in the virtual bilayer systems analyzed in this study.

Free-energy landscape of PITP α interactions with lipid. Previous electron spin resonance studies rationalized the ATP-independence of yeast Sec14-driven exchange cycle as a system where a PL molecule is engaged in a simple partitioning between two chemically similar microenvironments – i.e. the bilayer and the PITP PL-binding cavity [33,34]. The PITP α studies reported herein extend that concept. First, PITP α dramatically lowered the free energy of PL desorption from the bilayer to within the realm of thermal fluctuation. This lowering of an otherwise very significant thermodynamic barrier was driven by specific H-bond interactions between PITP α and lipid ligand headgroups.

Second, free energy profiles for PtdIns and PtdCho trajectories through the lipid binding pocket indicated that energy minima were shallow – thereby accounting for why PL molecules that had partially loaded, or were otherwise steered, into the PITP α pocket were spontaneously and efficiently released into the bilayer via a reverse

unloading reaction during simulation. This feature likely reflects the fact that no larger conformational transitions of the PITP from the open to the closed state were observed in those 1000ns simulations. Such conformational transitions would have the dual effects of dramatically impacting the free energy landscapes of the exchange cycle and would likely contribute to the purported 16-fold greater affinity of PITP α for PtdIns vs PtdCho. Such a marked difference in PITP α affinity for PtdIns vs PtdCho was not at all apparent in our calculations as those analyses reported the free energies of loading for both PLs to be similar.

In support of this idea, a solvent box-based MDS system that does model larger conformational motions of the PITP α molecule indicated that headgroup-specific conformational transitions within the C-terminal G-helix exerted headgroup-specific control of the PL-exchange cycle. This finding is interesting for two reasons. First, the G-helix does not contact bound PtdIns or PtdCho directly and is far removed from both headgroups. Second, the M₂₄₁T missense substitution in the G-helix selectively compromises PtdIns-transfer activity and represents a recognized SNP circulating in the human population.

PITP::PL interactions during the exchange cycle. Umbrella sampling data of PL ‘unloading’ provided novel insights into which PITP α residues play direct roles in facilitating PtdIns and PtdCho transit through the PITP α lipid binding pocket. Superposition of the structural elements and residues identified in this study to play important roles in the PITP α PL-exchange cycle, with primary sequences of other members of the StART-like PITP family, lend further confidence in the veracity of the data. MD simulations projected six residues of the PITP α lipid binding pocket interact with PtdIns (Thr₅₉, Lys₆₁, Glu₈₆, Asn₉₀, Thr₁₁₄, Glu₂₁₈) and, of those, all but Glu₂₁₈ are absolutely conserved in evolutionarily distant members of the larger StART-like PITP family (Figure 11). The one exception (Glu₂₁₈) is invariant among evolutionarily distant Class 1 StART-like PITPs. MD simulations also identified seven residues of the PITP α lipid binding pocket as engaging both PtdIns and PtdCho in H-bond

interactions (Tyr₁₈, Gln₂₂, Ser₂₅, Tyr₆₃, Asn₁₀₁, Lys₁₉₅, Gln₂₁₇). Of those, three are invariant (Tyr₁₈, Asn₂₂, Lys₁₉₅), one is invariant with a single exception involving a conserved substitution at that position (Tyr₆₃), and two others are invariant among the Class 1 StART-like PITP α s from primates to flies (Ser₂₅, Asn₁₀₁; Figure 11). This correspondence is remarkable given MDS are agnostic to experiment and to primary sequence alignments.

Of the set of identified specific interactions put to the functional test, the MD simulations were not absolutely accurate in their precise descriptions of headgroup-specific interactions. However, while the suggested lipid headgroup specificities were not borne out by experiment, the MD simulations did accurately identify these residues as important for optimal lipid exchange activity. The functional involvements of these residues in the exchange cycle were otherwise invisible to analyses of PITP α crystal structures alone.

If there are degrees of freedom for what residues are tolerated at these positions, why would those residues be so conserved across large evolutionary distances? We speculate that, while there might be compensating interactions that are permissive for PL-exchange in an *in vitro* system, strong evolutionary pressures are at play in cellular systems. For example, appropriate presentation of PtdIns to a PtdIns 4-OH kinase for biologically sufficient PtdIns-4-P production (i.e. in the face of cellular antagonists of PtdIns-4-P signaling) might demand stringent geometric requirements for PtdIns/PtdCho trajectories during the exchange cycle that are not apparent in *in vitro* lipid transfer assays.

Outstanding questions. While the studies reported here describe the initial steps in a pathway of conformational transition from an apo-PITP α to a phospholipid-bound holo-PITP α , and describe conformational transitions in the C-terminal G-helix that exhibit surprisingly long-range headgroup-specific involvements in the PL-exchange cycle, there remain outstanding considerations that will impact the details in important ways. First, the most productive MD simulations involved a membrane-docked PITP α conformer. At this point, it remains unknown how

PL-unloading is spatially or temporally related to PL-loading. That is, are these concerted processes, or are these separable reactions that proceed through an apo-PITP α intermediate? While soluble probe accessibility experiments argue against the latter mode (our unpublished data), the MD simulations reported here do not and cannot explicitly consider concerted PL-loading/unloading exchange mechanisms. Whether the PL-loading and unloading reactions are perfectly symmetrical processes also remains to be determined. Such symmetry is unlikely if PL-loading and unloading are concerted reactions. Finally, these simulations do not consider involvement of the PtdIns 4-OH kinase.

Those open questions notwithstanding, the satisfying congruence of the *in silico* data with the results of functional assays lends confidence that atomistic details of the PITP α PL-exchange reaction reported herein describe a reasonable first conceptualization of the initial stages of this key biological reaction. Extended MD production runs that capitalize on the membrane-docked apo- and holo-PITP α models described in this report now define promising approaches for linking the insights from the atomistic simulations of phospholipid loading/unloading by membrane-bound PITP α with insights culled from simulations of solvated PL-bound protein. We expect such extended simulations will extract new sets of fundamental mechanistic details regarding how the lipid-exchange cycle operates in StART-like PITP α s.

MATERIALS AND METHODS

Atomistic Molecular Dynamics Simulations.

Molecular dynamics simulations were performed for PITP α in a system reconstituted with a lipid bilayer consisting of either pure 1,2-dioleoyl-phosphatidylcholine (PtdCho) or a 90%/10% molar mixture of PtdCho and PtdIns. PITP α structures in the open (PDB 1KCM) and closed (PDB 1FVZ) conformations were retrieved from the RCSB Protein Data Bank [22,23]. The former structure is lipid-free whereas the latter describes PITP α in complex with a single bound PtdCho molecule. These two starting structures were each introduced into each of the two bilayer systems to generate a total of four distinct systems that were run in 1 μ s all-atom simulations. The simulations

were repeated 3 times for each system with different starting position of the protein in water solution above membrane, together resulting in 3 μ s of simulation time for each system, and in overall 12 μ s simulation time. In all cases, PITP α was initially positioned above the bilayer in the water phase. Simulations were run at physiological salt concentrations (150 mM KCl) and counter ions were introduced to neutralize the total charge of the system. Details of the compositions of each simulated system are provided in Supplementary Table S1.

The OPLS all-atom force field was used to describe all molecules [35]. For water, the TIP3P model that is compatible with the OPLS parameterization was employed [36]. The system structure used in this study is identical to those employed in our previous simulations of lipid bilayers [37,38]. To parameterize lipid molecules, parameters specifically derived for lipids were used [39-41]. Periodic boundary conditions with the usual minimum image convention were employed in all three dimensions. The length of each hydrogen atom covalent bond was preserved by the LINCS algorithm [42]. The integration time step was set to 2 fs and the simulations were carried out at constant pressure (1 bar) and temperature (310 K). The temperature and pressure were controlled by the Parrinello-Rahman and velocity-rescale methods, respectively [43,44]. The temperatures of the solute and the solvent were coupled separately. For pressure, a semi-isotropic scaling was employed. The Lennard-Jones interactions were cut off at 1.0 nm. For the electrostatic interactions, the particle mesh Ewald method [45] was employed with a real space cut-off at 1.0 nm, beta-spline interpolation (6th order), and a direct sum tolerance of 10^{-6} . The simulations were performed with the GROMACS 4.5.5 simulation package [46,47].

Molecular Dynamics Simulations of PITP in a Solvated System. Extensive (250 ns) molecular dynamics simulation (MDS) were carried out on PITP α structures prepared from: closed conformation bound to PtdCho (pdb i.d. 1T27: 2.20 Å), open conformation not bound to lipid (pdb i.d. 1KCM: 2.00 Å), and closed conformation complex with PtdIns (pdb i.d. 1UW5: 2.20 Å). From these available crystal structures, several

starting structures were generated in open conformation in combination with PtdCho and PtdIns. A total of 3 MD simulations were run for 250 ns each using the Desmond module of Schrodinger version 2016-3 (*D.E. Shaw, Schrodinger Inc.*), with the OPLS-AA forcefield as defined in Desmond. System Builder within Desmond/Schrodinger was used to generate a solvated system of protein-ligand complex. An orthorhombic box with a 12Å buffer around protein-ligand complex was used to generate the periodic box. An all atom atomistic scale MD simulation was carried out in a periodic box of explicit water molecules. For water, the TIP3P water model compatible with the OPLS-AA parameterization was employed. Simulation was carried out at 300K at a physiological salt concentration of 150 mM NaCl. Counter ions were included to neutralize the total charge of the system.

The OPLS-AA all atom force field was used to describe all molecules, and the system was relaxed using Maestro's system relaxation protocol before the production run. That regime included a multi-stage relaxation protocol with two stages of minimization with 5000 steps of restrained minimization and 5000 steps of unrestrained minimization followed by five stages of MD runs with gradually diminishing restraints on solute-heavy atoms. These stages include 500ps of restrained and 500ps of unrestrained equilibration under an NVT ensemble. The system was further equilibrated under NPT ensemble with 300ps of restrained equilibration, a 350ps of restrained equilibration at 300K with annealing off, and another 350ps of unrestrained equilibration at 300K. A separate MD production run of 250ns was carried out at constant temperature and pressure.

Long-range electrostatic interactions were estimated using the particle mesh Ewald, whereas bonds involving protons were constrained using the SHAKE algorithm [48]. A 2-fs time step was used throughout the simulation. The Thermostat Nose-Hoover chain method was applied with relaxation time of 1 ps [49]. Barostat parameters were set according to Martyna-Tobias-Klein [50] with a relaxation time of 2.0 ps with isotropic coupling. A 9Å cutoff was applied to Lennard-Jones interactions, and the nonbonded list was

updated every 1.2 ps. The production run was continued for 250 ns, and snapshots of the coordinates were written out every 1 ps. The results were analyzed and plots were generated within Maestro's Simulation Event Analysis and Simulation Interaction Diagram modules.

Free Energy Calculations. Free energies of PtdCho and PtdIns uptake by PITP α were obtained by umbrella sampling simulations of two model systems. The starting structure of the first system was obtained from the final structure after a 1 μ s production run of simulation1 of the system composed of the open PITP α and PtdCho bilayer (Supplementary Table S1 – system 3). The second system was generated from the first by replacing the PtdCho molecule positioned closest to the binding site with a PtdIns molecule.

Free energy profiles for PtdCho and PtdIns uptake by PITP α were calculated using the umbrella sampling method [51]. The starting structures were obtained as follows. First, a single PL (PtdCho or PtdIns) was pulled from the bilayer towards the PITP α lipid-binding pocket along the z-axis (membrane normal) in 20 ns simulation with a constant pulling force constant of 1000 kJ x mol⁻¹ x nm⁻² and pulling rate of 0.00075 nm x ns⁻¹ exerted on the lipid headgroup. Next, the position of the lipid headgroup was adjusted by lateral pulling such that it was positioned in the near vicinity of PITP α residues Cys₉₅ and Phe₂₂₅ reported to be important for PtdCho binding [22,52], or residues Thr₅₉, Lys₆₁, Glu₈₆, and Asn₉₀ known to coordinate the inositol headgroup [25,31]. After the PLs were optimally positioned within the PITP α binding pocket, the constraints imposed on the respective headgroups were released. The PtdCho and PtdIns systems were then simulated for an additional 150 and 240 ns, respectively.

In umbrella sampling simulations, 28 and 26 windows with a spacing of 0.1 nm were employed for PtdIns and PtdCho systems, respectively. The reaction coordinate (ζ) was chosen as z-coordinate of the lipid headgroup with boundaries at the plane of the membrane-water interface and at the upper regions of the lipid binding pocket. In each window, a harmonic restraining potential of 1000 kJ x mol⁻¹ x nm² was applied in the z-direction on

the distance between the center of mass of the given headgroup and the PtdCho bilayer bound with PITP α . Finally, the free energy profile for both PLs was constructed with the weighted histogram analysis method (WHAM) [53] based on the biased distribution of the given PL and magnitude of the umbrella biasing potential along the reaction coordinate. All free energy calculations were performed with an identical set of simulation parameters as described above for the equilibrium simulations.

Visualization. All the snapshots and movies presented in this work were prepared using the VMD package [54]. Molecular graphics and analyses of *Pitpna* single-nucleotide polymorphisms were performed with the UCSF Chimera package developed by the Resource for Biocomputing, Visualization, and Informatics at the University of California, San Francisco.

Lipid Reagents. For radiolabeled lipid transfer assays, preparation of [³H]-PtdIns rat liver microsomes has been described [1,17]. [³H]-PtdCho (L- α -dipalmitoyl [choline methyl-³H], ART 0284) was purchased from American Radiolabeled Chemicals, Inc. (ARC). For fluorescence-based lipid transfer assays, L- α -PtdCho and L- α -phosphatidic acid from chicken egg of highest available quality, were purchased from Avanti Polar Lipids (Alabaster, AL, USA), and used without further purification. 1-Palmitoyl-2-decapyrenyl-sn-glycero-3-phosphocholine (PyrPtdCho) was synthesized from 1-palmitoyl-2-hydroxy-sn-glycero-3-phosphocholine (Avanti Polar Lipids) and parinaroyl anhydride [55,56], and purified by reverse phase HPLC chromatography (Beckman Ultrasphere ODS outfitted with 4.6 x 25 cm column [57]). 1-Palmitoyl-2-decapyrenyl-sn-glycero-3-phosphoinositol (PyrPtdIns) was prepared from yeast PtdIns and parinaroyl anhydride as described [58]. 2,4,6-trinitrophenyl-phosphatidylethanolamine (TNP-PtdEtn) was prepared as described [59], and purified by silica gel column chromatography. Stock solutions of lipids were prepared in methanol and kept at -20 °C. The concentrations of PyrPtdIns and PyrPtdCho were determined spectroscopically, while the concentrations of L- α -PtdCho, L- α -

phosphatidic acid and TNP-PtdEtn solutions were determined according to Rouser et al. [60]. All lipid solutions were taken to ambient temperature before use. All other chemicals used were of highest available quality and the organic solvents were of spectroscopic grade.

Yeast strains and media. Yeast were grown in YPD liquid media (1% yeast extract, 2% bacto-peptone, and 3% glucose), or SD liquid media (0.67% nitrogen base, 3% glucose with appropriate amino acids supplemented) [60]. The respective plate media included 2% agar. Yeast strains CTY182 (*MATa ura3-52 lys2-801 Δhis3-200*), and CTY1-1A (*MATa ura3-52 lys2-801 Δhis3-200 sec14-1^{ts}*) were previously described [1,2,62]. *PITPNA*-expressing yeast strains were constructed by genomic integration of a single copy cassette where the *PITPNA* open reading frame was expressed under the control of the powerful and constitutive *PGK1* promoter (*P_{PGK}*) and configured in tandem with a functional *HIS3* selection marker. The integration cassette was recombined into the *LEU2* locus of the appropriate recipient yeast strain by standard lithium acetate transformation methods [62]. Transformants were selected on media lacking histidine and correct integration of the cassette was confirmed by screening for leucine auxotrophy as unselected phenotype. *PITPNA* over-expression strains were generated by transformation with the *PITPNA* expression cassette (driven by the powerful constitutive *PMA1* promoter) subcloned into a yeast *URA3* episomal plasmid pDR195 [63,64]. Transformants were selected on uracil-free media.

Site-directed mutagenesis. The *Rattus norvegicus* *PITPNA* gene was mutated by site-directed mutagenesis in the *P_{PGK1}-PITPNA HIS3* yeast *LEU2* integration cassette, the pDR195 (*P_{PMA1}-PITPNA*) vector, and in the pET28b-*His8-PITPNA* protein expression plasmid. Mutations were confirmed by DNA sequencing. Nucleotide sequences for primers the corresponding primers are available from the authors by request.

Protein purification. Recombinant PITP α and mutant versions were expressed from pET28b-*His8-PITPNA* vectors propagated in *E.coli* BL21 (RIL/DE3; New England BioLabs Inc, Ipswich,

MA). Bacteria were cultured in 4L TB + kanamycin/chloramphenicol media for 4hrs at 37°C, shifted to 16°C and induced for recombinant protein expression with IPTG (100 μ M final concentration). Cultures were harvested after 18hrs, and cells disrupted by passage through a French Press in low-phosphate lysis buffer (300mM NaCl, 25mM Na-phosphate, 5mM 2-mercaptoethanol, pH 7.5). Clarified lysates were incubated with TALON metal affinity beads (Clontech, Mountain View, CA), and bound proteins step-eluted with imidazole (25mM–200mM). Proteins were concentrated using the Amicon Ultra filter system (EMD Millipore), and concentration determined by SDS-PAGE and comparison against a BSA standard mass series.

Lipid transfer assays. End-point assays measured transport of [³H]-PtdIns from rat liver microsomes to PtdCho liposomes or [³H]-PtdCho from liposomes (98 mol% PtdCho, 2mol% PtdIns) to bovine heart mitochondria as described [1,17].

Pyrene-labeled PtdCho (PyrPtdCho) and PtdIns (PyrPtdIns) binding and transfer measurements were performed using a real-time de-quenching assay as described by Somerharju et al. [65] with modification. For the transfer measurements two vesicle populations were used. The donor (with TNP-PtdEtn quencher) and acceptor (without TNP-PtdEtn quencher) vesicles were prepared as follows. For the acceptor vesicles stock solutions of egg PtdCho and egg phosphatidic acid were mixed in a 291/9 nmol (97/3 mol%) ratio and dried under a stream of N₂. The resulting lipid film was then hydrated with 2 ml low phosphate buffer (25 mM Na₂HPO₄, 300 mM NaCl, pH 7.5) and sonicated on ice for 10 min. For the donor vesicles stock solutions of egg PtdCho, PyrPtdCho/PyrPtdIns and TNP-PtdEtn were mixed in a 4/0.5/0.5 nmol ratio, solvent was evaporated and the lipid film re-suspended in 10 μ l EtOH. The solution was injected into the buffer containing the acceptor vesicles. After a 5-10 min equilibrium period, the fluorescence intensity (excitation 346 nm, emission 378 nm) was measured as a function of time at 37°C using a ISS K2 fluorimeter (ISS Inc., Champaign, IL).

To measure transfer from donor to acceptor, 1 μ g protein was injected every 250 secs for a total of 4 injections. To obtain relative transfer

efficiency, the initial slope after each protein injection was calculated and the mean slope values for each protein (n=4) was normalized to that calculated for purified PITP α . For binding measurements, donor vesicles were injected into 2 ml low phosphate buffer. After a 5-10 min equilibrium period the solution was titrated 10x with 0.1 nmol recombinant protein and

fluorescence intensity was measured as a function of wavelength (excitation 343 nm, emission 360-450 nm) at 37 °C (K2 fluorimeter). The intensity at 348 nm was then plotted against protein amount and the slope value for each protein was calculated and normalized against PITP α in order to obtain the relative binding efficiency.

Acknowledgments: AG, ML, MIM, GS and VAB were supported by awards from the Robert A. Welch Foundation (BE-0017) and the National Institute of Health (RO1 GM112591) to VAB. AO, JV, MJ, TR and IV were supported by grants from the Academy of Finland, the Academy of Finland Center of Excellence program (IV), the European Research Council Advanced Grant CROWDED-PRO-LIPIDS (IV), and the Sigrid Juselius Foundation (IV). ML was supported by a postdoctoral fellowship from the Sigrid Juselius Foundation. We also extend our thanks to The Laboratory for Molecular Simulation and High Performance Research Computing (HPRC) at Texas A&M University for providing software, support and computer time. Development of the UCSF Chimera package was supported by NIGMS P41-GM103311.

Conflicts of interest: The authors have no financial conflicts to declare.

Author contributions: A.G. and A.O. were involved in all aspects of the experimentation and experimental design, data analysis, manuscript preparation, and production of figures. A.T. was involved in all aspect of computational experimental design of the membrane-free MDS, data analysis, manuscript preparation, and production of figures. A.O., J.V., M.J., T.R. designed and conducted MDS in bilayer-containing systems. A.G. and G.S. designed and performed the in vivo complementation experiments, and A.G. and M.L. designed and executed the in vitro lipid transfer and binding studies. P.S. synthesized the pyrene-labeled lipids used in this work. M.I.M. performed the mutant PITP stability assays. V.A.B and I.V. were involved in all aspects of experimental design, data analysis, and manuscript preparation.

REFERENCES

1. Bankaitis V.A., Aitken J.R., Cleves A.E., and Dowhan, W. (1990) An essential role for a phospholipid transfer protein in yeast Golgi function. *Nature* **347**, 561-562.
2. Cleves, A.E., McGee, T. P., Whitters, E. A., Champion, K. M., Aitken, J. R., Dowhan, W., Goebel, M., and Bankaitis, V.A. (1991) Mutations in the CDP-choline pathway for PL biosynthesis bypass the requirement for an essential PL transfer protein. *Cell* **64**, 789–800.
3. Wu, W.-I., Routt, S., Bankaitis, V.A., and Voelker, D. (2000) A new gene involved in transport-dependent metabolism of phosphatidylserine, *PSTB2/PDR17*, shares sequence similarity with the gene encoding the PI/PC-TP, Sec14p. *J. Biol. Chem.* **275**, 14446-14456.
4. Ren, J., Lin, C.P., Pathak, M., Temple, B.R.S., Nile, A.H., Mousley, C., Duncan, M.C., Eckert, D., Leiker, T.J., Ivanova, P.T., Milne, D.S., Murphy, R.S., Brown, H.A., Verdaasdonk, J., Bloom, K.S., Ortlund, E.A., Neiman, A.M., and Bankaitis, V.A. (2014) A phosphatidylinositol transfer protein integrates phosphoinositide signaling with lipid droplet metabolism to regulate a developmental program of nutrient stress-induced membrane biogenesis. *Mol. Biol. Cell* **25**, 712-727.
5. Vincent, P., Chua, M., Nogue, F., Fairbrother, A., Mekeel, H., Xu, Y., Allen, N., Bibikova, T.N., Gilroy, S., and Bankaitis, V.A. (2005) A Sec14p-nodulin domain phosphatidylinositol transfer protein polarizes membrane growth of *Arabidopsis thaliana* root hairs. *J. Cell Biol.* **168**, 801– 812.
6. Huang, J., Kim, C.M., Xuan, Y.H., Park, S.J., Piao, H.L., Je, B.I., Liu, J., Kim, T.H., Kim, B.K., and Han, C.D. (2013) OsSNDP1, a Sec14-nodulin domain-containing protein, plays a critical role in root hair elongation in rice. *Plant Mol Biol* **82**, 39-50.
7. Ghosh, R., de Campos, M.K.F., Huang, J., Hur, S., Orłowski, A., Yang, Y., Tripathi, A., Nile, A.H., Lee, H.-C., Schäfer, H., Dynowski, M., Røg, T., Lete, M.G., Ahyayauch, H., Alonso, A., Vattulainen, I., Igumenova, T.I., Schaaf, G., and Bankaitis, V.A. (2015) Sec14-nodulin proteins and the patterning of phosphoinositide landmarks for developmental control of membrane morphogenesis. *Mol. Biol. Cell* **26**, 1764-1781.
8. Vihtelic, T.S., Hyde, D.R., and O'Tousa, J.E.(1991) Isolation and characterization of the *Drosophila* retinal degeneration B (rdgB) gene. *Genetics* **127**, 761–768.
9. Milligan, S.E., Alb, J.G., Jr., Elagina, R., Bankaitis, V.A., and Hyde, D.R. (1997) The phosphatidylinositol transfer protein domain of *Drosophila* retinal degeneration protein B is required for photoreceptor cell survival and recovery from light stimulation. *J. Cell Biol.* **139**, 351-363.
10. Giansanti, M.G., Bonaccorsi, S., Kurek, R., Farkas, R.M., Dimitri, P., Fuller, M.T., and Gatti, M. (2006) The class I PITP giotto is required for *Drosophila* cytokinesis. *Curr. Biol.* **16**, 195-201.
11. Ile, K.E., Kassen, S., Cao, C., Vihtelic, T., Shah, S.D., Huijbregts, R.P.H., Alb, J.G., Jr., Stearns, G.W., Brockerhoff, S.E., Hyde, D.R., and Bankaitis, V.A. (2010) The zebrafish class 1 phosphatidylinositol transfer protein family: PITP α isoforms and double cone cell outer segment integrity in retina. *Traffic* **11**, 1151-1167.
12. Hamilton, B.A., Smith, D.J., Mueller, K.L., Kerrebrock, A.W., Bronson, R.T., van Berkel, V., Daly, M.J., Kruglyak, L., Reeve, M.P., Nemhauser, J.L., Hawkins, T.L., Rubin, E.M., and Lander, E.S. (1997) The *vibrator* mutation causes neurodegeneration via reduced expression of PITP α : Positional complementation cloning and extragenic suppression. *Neuron* **18**, 711-722.
13. Alb J.G. Jr., Cortese J.D., Phillips S.E., Albin R.L., Nagy T.R., Hamilton B.A., and Bankaitis V.A. (2003) Mice lacking phosphatidylinositol transfer protein-alpha exhibit spinocerebellar degeneration, intestinal and hepatic steatosis, and hypoglycemia. *J. Biol. Chem.* **278**, 33501-33518.
14. Alb, J.G. Jr., Phillips, S.E., Wilfley, L.R., Philpot, B.D., and Bankaitis, V.A. (2007) The pathologies associated with functional titration of phosphatidylinositol transfer protein α activity in mice. *J. Lipid Res.* **48**, 1857-1872.
15. Helmkamp, G.M., Harvey, M.S., Wirtz, K.W.A., and van Deenen, L.L.M. (1974) Phospholipid exchange between membranes. *J. Biol. Chem.* **249**, 6382-6389.
16. Wirtz, K.W.A. (1991) Phospholipid transfer proteins. *Annu. Rev. Biochem.* **60**, 73-99.

17. Schaaf, G., Ortlund, E., Tyeryar, K., Mousley, C., Ile, K., Woolls, M., Garrett, T., Raetz, C.R.H., Redinbo, M., and Bankaitis, V.A. (2008) The functional anatomy of PL binding and regulation of phosphoinositide homeostasis by proteins of the Sec14-superfamily. *Molecular Cell* **29**, 191-206.
18. Bankaitis, V.A., Mousley, C.J., and Schaaf, G. (2010) The Sec14-superfamily and mechanisms for crosstalk between lipid metabolism and lipid signaling. *Trends in Biochem. Sci* **35**, 150-160.
19. Grabon, A., Khan, D., and Bankaitis, V.A. 2015. Phosphatidylinositol transfer proteins and instructive regulation of lipid kinase biology. *Biochim Biophys Acta* **1851**, 724-735.
20. Ryan, M.M., Temple, B.R.S., Phillips, S.E., and Bankaitis, V.A. (2007) Conformational dynamics of the major yeast phosphatidylinositol transfer protein Sec14: Insights into the mechanisms of PL exchange and diseases of Sec14-like protein deficiencies. *Mol. Biol. Cell* **18**, 1928-1942.
21. Schaaf, G., Dynowski, M., Mousley, C.J., Shah, S.D., Yuan, P., Winklbauer, E.M., de Campos, M.K.F., Trettin, K., Quinones, M.C., Smirnova, T., Yanagisawa, L.L., Ortlund, E.A., and Bankaitis, V.A. (2011) Resurrection of a functional phosphatidylinositol transfer protein from a pseudo-Sec14 scaffold by directed evolution. *Mol. Biol. Cell* **22**, 892-905.
22. Yoder, M.D., Thomas, L.M., Tremblay, J.M., Oliver, R.L., Yarbrough, L.R., and Helmkamp Jr., G.M. (2001) Structure of a multifunctional protein. Mammalian phosphatidylinositol transfer protein complexed with phosphatidylcholine. *J. Biol. Chem.* **276**, 9246-9252.
23. Schouten, A., Agianian, B., Westerman, J., Kroon, J., Wirtz, K.W., and Gros, P. (2002) Structure of apo-phosphatidylinositol transfer protein alpha provides insight into membrane association. *EMBO J.* **21**, 2117-2121.
24. Kabsch, W., and Sander, C. (1983) Dictionary of protein secondary structure: Pattern recognition of hydrogen-bonded and geometrical features. *Biopolymers* **22**, 2577-637.
25. Tilley S.J., Skippen A., Murray-Rust J., Swigart P.M., Stewart A., Morgan C.P., Cockcroft S., and McDonald, N.Q. (2004) Structure-function analysis of phosphatidylinositol transfer protein alpha bound to human phosphatidylinositol. *Structure* **12**, 317-326.
26. Yadav, S., Garner, K., Georgiev, P., Li, M., Gomez Espinosa, E., Panda, A., Mathre, M., Cockcroft, S., and Raghu, P. (2015) RDGB α , a PtdIns-PtdOH transfer protein, regulates G-protein-coupled PtdIns(4,5)P $_2$ signalling during Drosophila phototransduction. *J.Cell.Sci.* **128**, 3330-3344.
27. Phillips, S.E., Ile, K., Boukhelifa, M., Huijbrechts, R.P.H., and Bankaitis, V.A. (2006) Specific and nonspecific membrane binding determinants cooperate in targeting phosphatidylinositol transfer protein β -isoform to the murine *trans*-Golgi network. *Mol. Biol. Cell* **17**, 2498-2512.
28. Lomize, M. A., Pogozheva, I. D., Joo, H., Mosberg, H. I., and Lomize, A. L. (2012) OPM database and PPM web server: resources for positioning of proteins in membranes. *Nucleic Acids Research*, **40**, D370-D376.
29. Skinner, H.B., Alb Jr., J.G., Whitters, E.M., Helmkamp Jr., G.M., and Bankaitis, V.A. (1993) Phospholipid transfer activity is relevant to but not sufficient for the essential function of the yeast SEC14 gene product. *EMBO J.* **12**, 4775-4784.
30. Palonciová, M., Berka, K., and Otyepka, M. (2012) Convergence of the free energy profile of coumarin in lipid bilayer. *J. Chem. Theory Comput.* **8**, 1200-1211.
31. Alb, J.G. Jr., Gedvilaite A., Cartee R.T., Skinner H.B., and Bankaitis V.A. (1995) Mutant rat phosphatidylinositol/phosphatidylcholine transfer proteins specifically defective in phosphatidylinositol transfer: implications for the regulation of phosphatidylinositol transfer activity. *Proc. Natl. Acad. Sci. USA* **92**, 8826-8830.
32. Lek, M., Karczewski, K. J., Minikel, E. V., Samocha, K. E., Banks, E., Fennell, T., O'Donnell-Luria, A. H., Ware, J. S., Hill, A. J., Cummings, B. B., Tukiainen, T., Birnbaum, D. P., Kosmicki, J. A., Duncan, L. E., Estrada, K., Zhao, F., Zou, J., Pierce-Hoffman, E., Berghout, J., Cooper, D. N., Deflaux, N., Depristo, M., DO, R., Flannick, J., Fromer, M., Gauthier, L., Goldstein, J., Gupta, N., Howrigan, D., Kiezun, A., Kurki, M. I., Moonshine, A. L., Natarajan, P., Orozco, L., Peloso, G. M., Poplin, R., Rivas, M. A., Ruano-Rubio, V., Rose, S. A., Ruderfer, D. M., Shakir, K., Stenson, P. D., Stevens, C., Thomas, B. P., Tiao, G., Tusie-Luna, M. T., Weisburd, B., Won, H.-H., YU, D., Altshuler, D. M., Ardissino, D.,

- Boehnke, M., Danesh, J., Donnelly, S., Elosua, R., Florez, J. C., Gabriel, S. B., Getz, G., Glatt, S. J., Hultman, C. M., Kathiresan, S., Laasko, M., McCarroll, S., McCarthy, M. I., McGovern, D., McPherson, R., Neale, B. M., Palotie, A., Purcell, S. M., Saleheen, D., Scharf, J. M., Sklar, P., Sullivan, P. F., Tuomilehto, J., Tsuang, M. T., Watkins, H. C., Wilson, J. G., Daly, M. J., MacArthur, D. G., and Exome Aggregation Consortium. (2016) Analysis of protein-coding genetic variation in 60,706 humans. *Nature*, **536**, 285-291.
33. Smirnova, T., Chadwick, T.G., MacArthur, R., Poluekov, O., Song, L., Ryan, M., Schaaf, G., and Bankaitis, V.A. (2006) The chemistry of PL binding by the *Saccharomyces cerevisiae* phosphatidylinositol transfer protein Sec14 as determined by electron paramagnetic resonance spectroscopy. *J. Biol. Chem.* **281**, 34897-34908.
34. Smirnova, T., Chadwick, T.G., Voinov, M.A., Poluektov, O., van Tol, J., Ozarowski, A., Schaaf, G., Ryan, M.M., and Bankaitis, V.A. (2007) Local polarity and hydrogen bonding inside the Sec14 PL-binding cavity: High-field multifrequency studies. *Biophys. J.* **92**, 3686-3695.
35. Jorgensen, W. L., and Tirado-Rives, J. (1988) The OPLS (optimized potentials for liquid simulations) potential functions for proteins, energy minimizations for crystals of cyclic peptides and crambin. *J. Am. Chem. Soc.* **110**, 1657-1666.
36. Jorgensen, W. L., Chandrasekhar, J., Madura, J. D., Impey, R. W., and Klein, M. L. (1983) Comparison of simple potential functions for simulating liquid water. *J. Chem. Phys.* **79**, 926.
37. Kaiser, H.J., Orłowski, A., Rog, T., Nyholm, T.K.M., Chai, W., Feizi, T., Lingwood, D., Vattulainen, I., and Simons, K. (2011) Lateral sorting in model membranes by cholesterol-mediated hydrophobic matching. *Proc. Natl. Acad. Sci. U.S.A.* **108**, 16628-16633.
38. Orłowski, A., St.-Pierre, J.F., Magarkar, A., Bunker, A., Pasenkiewicz-Gierula, M., Vattulainen, I., and Róg, T. (2011) Properties of the membrane binding component of catechol-O-methyltransferase revealed by atomistic molecular dynamics simulations. *J. Phys. Chem. B* **115**, 13541-13550.
39. Maciejewski, A., Pasenkiewicz-Gierula, M., O. Cramariuc, O., Vattulainen, I., and Róg, T. (2014) Refined OPLS-AA force field for saturated phosphatidylcholine bilayers at full hydration. *J. Phys. Chem. B.* **118**, 4571-4581.
40. Kulig, W., Pasenkiewicz-Gierula, M., and Róg, T. (2015) Topologies, structures and parameter files for lipid simulations in GROMACS with the OPLS-aa force field: DPPC, POPC, PtdCho, PEPC, and cholesterol. *Data in Brief* **5**, 333-336.
41. Kulig, W., Pasenkiewicz-Gierula, M., and Róg, T. (2016) Cholesterol interactions with *Cis* and *Trans* unsaturated phosphatidylcholines. Molecular dynamics simulation study. *Chem. Phys. Lipids.* **195**, 12-20.
42. Hess, B., Bekker, H., Berendsen, H.J.C., and Fraaije, J.G.E.M. (1997) LINCS: A linear constraint solver for molecular simulations. *J. Computational Chem.* **18**, 1463-1472.
43. Parrinello, M., and Rahman, A. (1981) Polymorphic transitions in single crystals: A new molecular dynamics method. *J. Applied Physics* **52**, 7182.
44. Bussi, G., Donadio, D., and Parinello, M. (2007) Canonical sampling through velocity rescaling. *J. Chem. Phys.* **126**, 014101.
45. Essmann, U., Perera, L., Berkowitz, M.L., Darden, T., Lee, H., and Pedersen, L.G. (1995) A smooth particle mesh Ewald method. *J. Chem. Phys.* **103**, 8577-8593.
46. Hess, B., Kutzner, C., van der Spoel, D., and Lindahl, E. (2008) GROMACS 4: Algorithms for highly efficient, load-balanced, and scalable molecular simulations. *J. Chem. Theory Comput.* **4**, 435-447.
47. Pronk, S., Páll, S., Schulz, R., Larsson, P., Bjelkmar, P., Apostolov, R., Shirts, M.R., Smith, J.C., Kasson, P.M., van der Spoel, D., Hess, B., and Lindahl, E. (2013) GROMACS 4.5: a high throughput and highly parallel open source molecular simulation toolkit. *Bioinformatics* **29**, 845-854.
48. Ryckaert, J. P., Ciccotti, G., and Berendsen, H. J. C. (1977) Numerical integration of the cartesian equations of motion of a system with constraints: molecular dynamics of *n*-alkanes. *J. Comp. Phys.* **23**, 327-341.

49. Martyna, G. J., Klein, M. L., and Tuckerman, M. (1992) Nosé–Hoover chains: the canonical ensemble via continuous dynamics. *J. Chem. Phys.* **97**, 2635–2643.
50. Martyna, G. J., Tobias, D. J., and Klein, M.L. (1994) Constant pressure molecular dynamics algorithms. *J Chem Phys J. Chem. Phys.* **101**, 4177–4189.
51. Kästner, J. (2011) Umbrella sampling. *Wiley Interdisciplinary Reviews: Computational Molecular Science* **1**, 932-942.
52. Garner, K, Hunt, A.N., Koster, G., Somerharju, P., Groves, E., Li, M., Raghu, P., Holic, R., and Cockcroft, S. (2012) Phosphatidylinositol transfer protein, cytoplasmic 1 (PITPNC1) binds and transfers phosphatidic acid. *J Biol Chem.* **287**, 32263-32276.
53. Kumar, S., Rosenberg, J.M., Bouzida, D., Swenden, R.H., and Kollman, P.A. (1992) The weighted histogram analysis method for free-energy calculations on biomolecules. I. The method. *J. Computational Chem.* **13**, 1011-1021.
54. Humphrey, W., Dalke, A., and Schulten, K. (1996) VMD: visual molecular dynamics. *J. Mol. Graph.* **14**, 33-38.
55. Salinger, Z., and Lapidot, Y. (1966) Synthesis of fatty acid anhydrides by reaction with dicyclohexylcarbodiimide. *J. Lipid. Res.* **7**, 174-175.
56. Gupta, C.M., Radhakrishnan, R., and Khorana, H.G. (1977) GlyceroPL synthesis: improved general method and new analogs containing photoactivable groups. *Proc. Natl. Acad. Sci. U.S.A.* **74**, 4315-4319.
57. Patton, G.M., Fasulo, J.M., and Robins, S.J. (1982) Separation of PLs and individual molecular species of PLs by high-performance liquid chromatography. *J. Lipid. Res.* **23**, 190-196.
58. Somerharju, P., and Wirtz, K.W.A. (1982) Semisynthesis and properties of a fluorescent phosphatidylinositol analogue containing a cis-parinaoyl moiety. *Chem. Phys. Lipids* **30**, 81-91.
59. Gordesky S.E., and Marinetti, G.V. (1973) The asymmetric arrangement of PLs in the human erythrocyte membrane. *Biochem. Biophys. Res. Commun.* **50**, 1027-1031.
60. Rouser, G., Fkeischer, S., and Yamamoto, A. (1970) A two dimensional thin layer chromatographic separation of polar lipids and determination of PLs by phosphorus analysis of spots. *Lipids* **5**, 494-496.
61. Sherman, F., Fink, G. R., and Hicks, J. B. (1983) *Methods in Yeast Genetics*, Cold Spring Harbor, NY: Cold Spring Harbor Laboratory: 1-113.
62. Bankaitis, V.A., Malehorn, D.E., Emr, S.D., and Greene, R. (1989) The *Saccharomyces cerevisiae* *SEC14* gene encodes a cytosolic factor that is required for transport of secretory proteins from the yeast Golgi complex. *J. Cell Biol.* **108**, 1271-1281.
63. Gietz, R.D., and Woods, R.A. (2002) Transformation of yeast by lithium acetate/single-stranded carrier DNA/polyethylene glycol method. *Methods Enzymol.* **350**, 87–96.
64. Rentsch, D., Laloi, M., Rouhara, I., Schmelzer, E., Delrot, S., and Frommer, W.B. (1995) NTR1 encodes a high affinity oligopeptide transporter in *Arabidopsis*. *FEBS Lett.* **370**, 264-268.
65. Somerharju, P.J., van Loon, D., and Wirtz, K.W. (1987) Determination of the acyl chain specificity of the bovine liver phosphatidylcholine transfer protein. Application of pyrene-labeled phosphatidylcholine species. *Biochemistry* **26**, 7193–7199.

FIGURE LEGENDS

Figure 1. Molecular dynamics of PITP α on membranes. **(A)** Crystal structures of the closed PtdCho-bound PITP α conformer (PDB: 1T27) and the open apo-PITP α conformer (PDB: 1KCM) with substructures color-coded and labeled (purple: regulatory loop, cornflower blue: lipid binding floor, dark blue: Helix A, cyan: Helix F, pink: Helix G, orange: lipid exchange loop). Membrane association regions identified by the MD simulations described in the text (MAR1: residues 28-41, MAR2: residues 99-110) are circled in dotted black on the open PITP structure. **(B)** Root mean square deviation (RMSD) of closed (two upper panels) and open PITP α conformers (two lower panels) in MD simulations, on PtdCho (left) or PtdCho/PtdIns (right) bilayers. **(C)** Root mean square fluctuation (RMSF) of open (right) and closed (left) PITP α conformers in MD simulations, on PtdCho (top) or PtdCho/PtdIns (bottom) bilayers. In each panel, analyses of each of three independent repeats are shown in different colors (black - simulations I, red - simulation II and green - simulation III).

Figure 2. Association of PITP α with the membrane over the simulation time course. Initial (0 μ s) and final (1 μ s) snapshots from the simulations of systems: 1 (closed PITP, membrane without PtdIns), 2 (closed PITP, membrane with PtdIns), 3 (open PITP, membrane without PtdIns) and 4 (open PITP, membrane with PtdIns), as described in Supplementary Table S1. Lipids are shown in licorice (PtdIns in yellow and PtdCho inside the binding pocket of PITP in red) and transparent brown surface. PITP α is rendered in new cartoon representation in colors corresponding to secondary structure (yellow: β -sheet, purple: α -helix, blue: 3_{10} -helix, cyan: random coil). Water molecules and ions are omitted for purpose of clarity.

Figure 3. Conformational changes of PITP α during the simulation. **(A)** Initial (0 μ s) and **(B)** final (1 μ s) snapshots from simulation system 4 using the open PITP α conformer as starting structure (Supplementary Table S1). The loop consisting of residues 25-38 is depicted in red, residues Ser₃₀ and Glu₄₁ are in orange licorice representation, and the indicated distance between their C α atoms is marked as a dashed black double-headed arrow. The lipid exchange loop is colored in green, and its conformational change between a turn (red highlight) and a 3_{10} helix (blue highlight) is indicated. The PtdCho lipid engaged by the lipid exchange loop is in yellow licorice representation. Snapshot from simulation system 4 (as described in Supplementary Table S1) of the open PITP α conformer in **(C)** new cartoon representation or **(D)** blue surface representation, where a PtdCho molecule (in licorice representation) is engaged by the lipid exchange loop in the final (1 μ s) step. Other lipids are shown as brown sticks, and water molecules and ions are omitted for clarity.

Figure 4. Functional consequences of missense substitutions for PITP α residue Ser₂₅. **(A)** Phenotypic rescue assays. Isogenic *SEC14* (CTY182; *MATa ura3-52, lys2-801, his3 Δ 200*) and *sec14-1^{ts}* strains (CTY1-1A; *MATa ura3-52, lys2-801, his3 Δ 200, sec14-1^{ts}*) served as positive and negative controls for PITP α activity, respectively. The latter strain fails to grow at 37°C because activity of the major PITP is inactivated at that temperature [29]. Isogenic *sec14-1^{ts}* yeast strains carrying expression cassettes for *RnPITPNA*, or versions carrying the indicated substitutions for residue Ser₂₅, integrated at the *LEU2* locus, were spotted in 10-fold dilution series onto YPD agar plates and incubated at either permissive temperature of 30°C or restrictive temperature of 37°C for 48 hours. **(B)** Endpoint PtdIns and PtdCho transfer assays. Purified recombinant PITP α and indicated missense mutants (10 μ g protein per assay) were assayed for [³H]-PtdIns and [³H]-PtdCho transfer, as indicated. Transfer efficiencies of PITP α were set at 100% (n=3), and transfer of mutant PITP α proteins are normalized relative to PITP α activity values obtained from the same experiments. Assay efficiencies and backgrounds for these experiments are summarized in Supplementary Table S5. **(C)** Rates of PyrPtdIns and PyrPtdCho-transfer were measured

for the indicated Ser₂₅ substitution mutants. Fluorescence intensities of PyrPtdIns or PyrPtdCho are plotted as a function of time. Black arrows mark addition of 1 μg increment of the indicated protein. Following protein addition, the observed increase in fluorescence intensity was directly proportional to the relative transfer efficiency of the protein being assayed. The initial slope after each addition was calculated to obtain relative transfer efficiencies (Supplementary Table S6). Error bars were calculated from two independent determinations.

Figure 5. Steered molecular dynamics simulation of PL in the PITPα binding pocket. Snapshots of the lipid unloading after the release of pulling force on the lipid (highlighted in bright green). Individual panels correspond to: **(A)** ~0 ns, ~75 ns, ~100 ns, and ~150 ns after the release of pulling force. Lipids are shown in licorice and PITPα in new cartoon representation. For purpose of clarity, water molecules and ions are not shown. **(B)** Left: Snapshot from one of the umbrella sampling simulations windows showing PtdCho (green VdW spheres) being unloaded back into the membrane by PITPα (new cartoon representation). Vertical axis represents the reaction coordinate ζ (nm) where $\zeta = 0$ nm corresponds to the midplane of the lipid bilayer, $\zeta = 2$ nm and $\zeta = 4$ nm correspond to the membrane-water interface and the upper part of the binding pocket, respectively. The horizontal gray helplines define the boundaries for lipid movement. Right: free energy profiles for PtdCho (red) and PtdIns (blue) uptake/unload. **(C)** Left: PITPα and amino acid residues that form H-bonds with PtdCho and/or PtdIns. Residue projected to interact predominantly with PtdCho is depicted in red (Lys₆₈), only with PtdIns in yellow (Lys₆₁, Glu₈₆, Asn₉₀, Thr₁₁₄, Glu₂₁₈), and in green residues that form H-bonds with both of the ligands (Tyr₁₈, Gln₂₂, Ser₂₅, Tyr₆₃, Asn₁₀₁, Lys₁₉₅, Gln₂₁₇). Right: Average number of H-bonds interactions between PITPα and PtdCho (red) and PtdIns (blue), as indicated, as a function of time. Profiles are calculated as a function of the umbrella window which has been translated into the reaction coordinate ζ (nm). The number of hydrogen bonds was calculated by counting all hydrogen bonds formed by a given residue, divided by the number of analyzed snapshots.

Figure 6. Functional consequences of missense substitutions for PITPα residue Lys₆₈. **(A)** Details of the phenotypic rescue assays for mutant PITPα versions carrying the indicated substitutions for Lys₆₈, and the organization of this Figure, are described in the legend to Figure 3A. **(B)** Endpoint PtdIns and PtdCho transfer assays using purified recombinant PITPα and indicated missense mutants, and organization of the Figure, are detailed in the legend to Figure 3B. Rates of PyrPtdIns and PyrPtdCho-transfer **(C)**, and efficiencies of PyrPtdIns and PyrPtdCho-binding **(D)** were measured for the indicated Lys₆₈ substitution mutants. Experimental details are as described in Figure 3C.

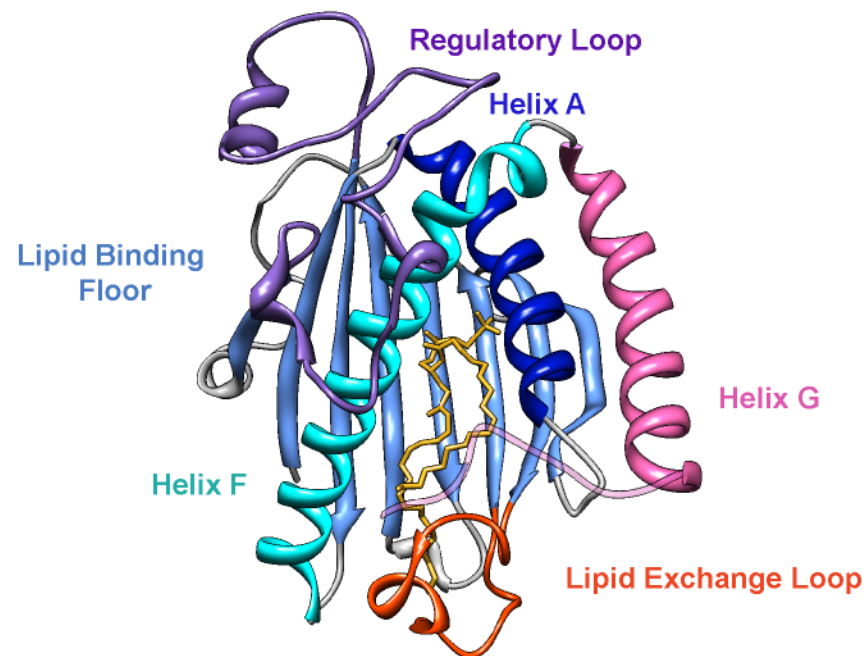
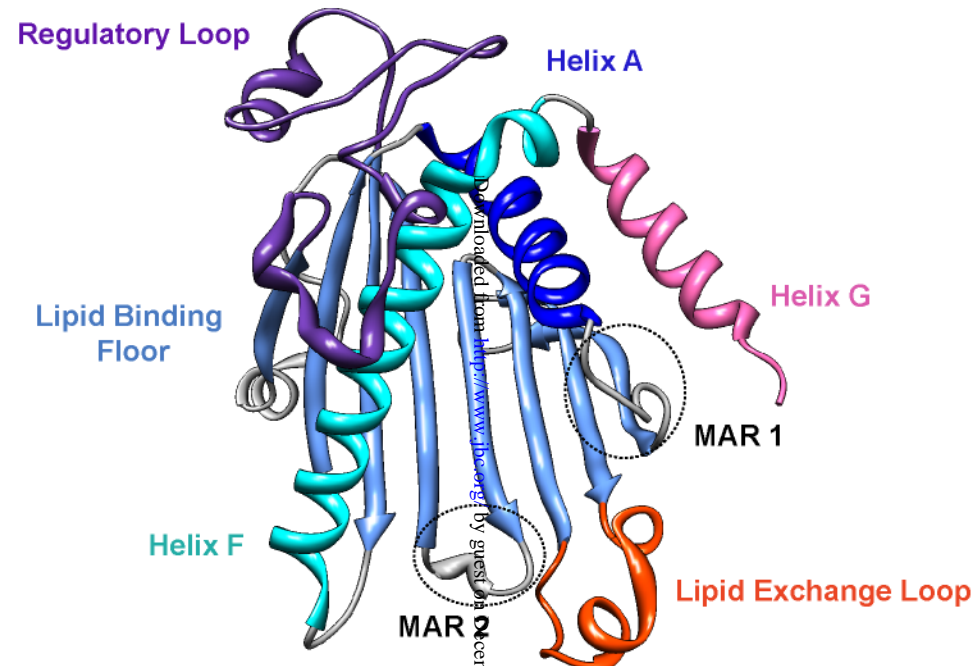
Figure 7. Functional consequences of missense substitutions for PITPα residue Glu₂₁₈. **(A)** Details of the phenotypic rescue assays for mutant PITPα versions carrying the indicated substitutions for Glu₂₁₈, and the organization of this Figure, are described in the legend to Figure 3A. **(B)** Endpoint PtdIns and PtdCho transfer assays using purified recombinant PITPα and indicated missense mutants, and organization of the Figure, are detailed in the legend to Figure 3B. Rates of PyrPtdIns and PyrPtdCho-transfer **(C)**, and efficiencies of PyrPtdIns and PyrPtdCho-binding **(D)** were measured for the indicated Glu₂₁₈ substitution mutants. Experimental details are as described in Figure 3C.

Figure 8. Functional consequences of missense substitutions for PITPα residue Lys₁₉₅. **(A)** Details of the phenotypic rescue assays for mutant PITPα versions carrying the indicated substitutions for Lys₁₉₅, and the organization of this Figure, are described in the legend to Figure 3A. **(B)** Endpoint PtdIns and PtdCho transfer assays using purified recombinant PITPα and indicated missense mutants, and organization of the Figure, are detailed in the legend to Figure 3B. Rates of PyrPtdIns and PyrPtdCho-transfer **(C)**, and efficiencies of PyrPtdIns and PyrPtdCho-binding **(D)** were measured for the indicated Lys₁₉₅ substitution mutants. Experimental details are as described in Figure 3C.

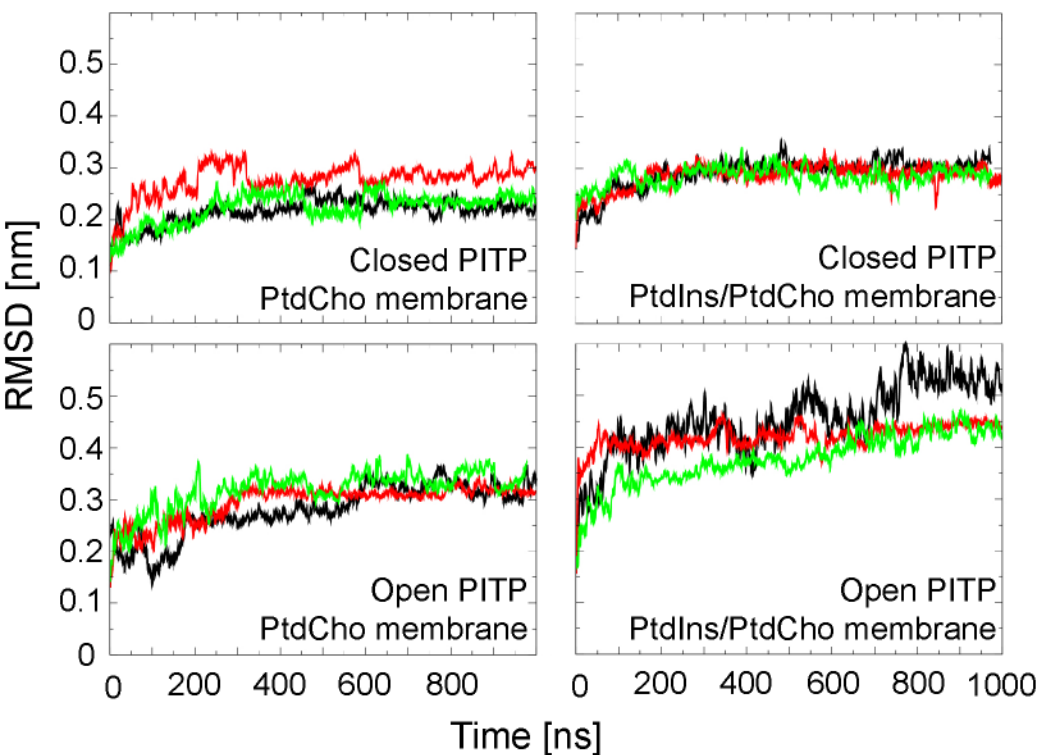
Figure 9. Molecular dynamics of PITP α open conformer G-helix in a solvent box. Snapshots (110ns) are shown from the MDS of (A) PITP α ::PtdCho, and (B) PITP α ::PtdIns. Blow-ups of the corresponding G-helices are shown to the right of the corresponding PITP α ::PL structures. PITP α is illustrated in blue ribbon render with the G-helix shown in green and key residues shown in stick model. PtdCho and PtdIns are illustrated in stick render. (C) Simulated van der Waals interactions apparent at 110ns of simulation of PITP α ::PtdIns between G-helix residues Met₂₄₁, Ile₂₄₄ and the A-helix residue Leu₂₃ are shown. A magnified A-helix is shown in orange and the G-helix in green with interacting residues in CPK rendering at right of the PITP α ::PtdIns structure.

Figure 10. PtdIns-selective defects associated with missense substitutions for PITP α residue Glu₂₄₈ or Met₂₄₁. (A) Details of the phenotypic rescue assays for mutant PITP α carrying the indicated substitutions for Glu₂₄₈, and the organization of this Figure, are described in the legend to Figure 3A. (B) Endpoint PtdIns and PtdCho transfer assays. Purified recombinant PITP α and indicated missense mutants, and organization of the Figure, are detailed in the legend to Figure 3B. Rates of PyrPtdIns and PyrPtdCho-transfer (C), and efficiencies of PyrPtdIns and PyrPtdCho-binding (D) were measured for the indicated Glu₂₄₈ or Met₂₄₁ substitution mutants. Experimental details are as described in Figure 3C.

Figure 11. Primary sequence alignments of selected regions of Class I and Class II StART-like PITPs. Sequences for PITP genes were extracted from the NCBI database using the following protein accession numbers: RnPITPNA (NP_058927.1), HsPITPNA (NP_006125.1), HsPITPNB (NP_036531.1), DmVibrator (NP_524404), HsPITPNC1 (NP_858057), HsPITPNM1 (NP_004901.2), HsPITPNM2 (NP_065896.1). For the multi-domain PITPs HsPITPNM1 and HPITPNM2, only the PITP domain primary sequence is included in the alignment as guided by primary sequence homology to HsPITP α . Alignments were generated in VectorNTI using the AlignX module set to default parameters, and visualized using UGENE. Indicated at bottom for purposes of reference are residue numbers according the RnPITP α primary sequence. Color coding follows UGENE homology descriptors, where identical residues are on dark blue background, non-similar residues are on white background, and highly or weakly conserved residues fall in between on the blue background gradient. Residues predicted by MD to have predominantly PtdIns-specific interactions (*) include Thr₅₉, Lys₆₁, Glu₈₆, Gln₉₀, Thr₁₁₄, and Glu₂₁₈; predominantly PtdCho-specific interactions (#) include Lys₆₈; and interactions with both PtdIns and PtdCho (+) include Tyr₁₈, Gln₂₂, Ser₂₅, Tyr₆₃, Gln₁₀₀, Lys₁₉₅, and Gln₂₁₇. Residues Met₂₄₁ and Glu₂₄₈ have specific roles in PtdIns-transfer via a mechanism that does not involve direct phospholipid binding, and these residues are highlighted by (X) at top.

Figure 1**A**PITP α ::PtdCho, ClosedPITP α , Open**B**

— simulation 1 — simulation 2 — simulation 3

**C**

— simulation 1 — simulation 2 — simulation 3

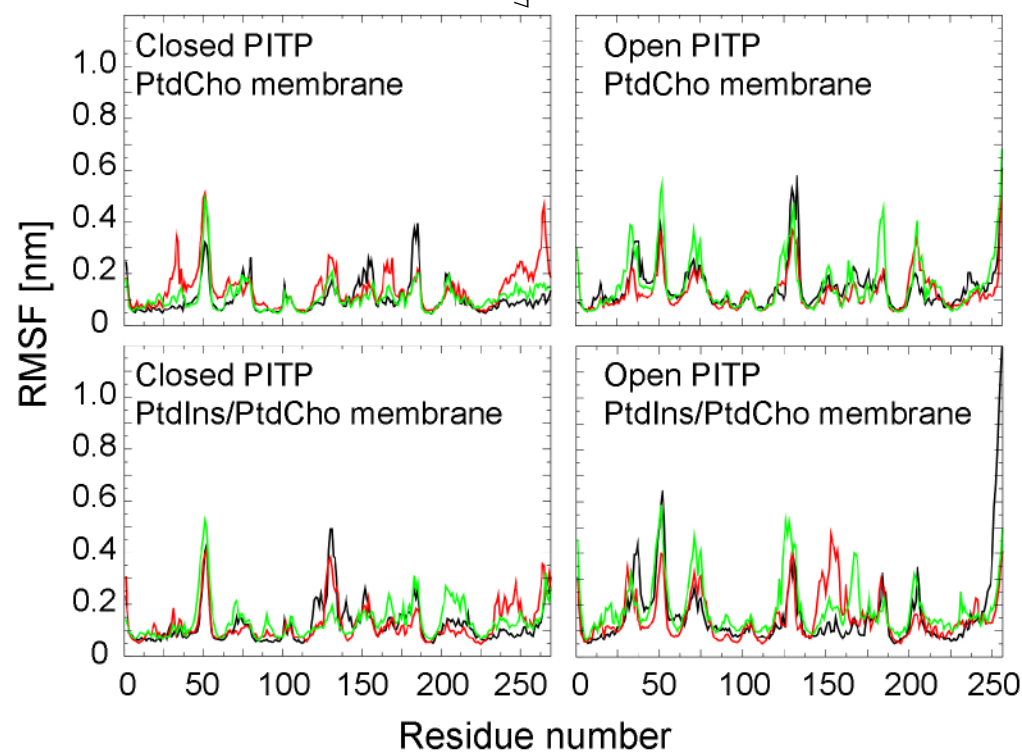
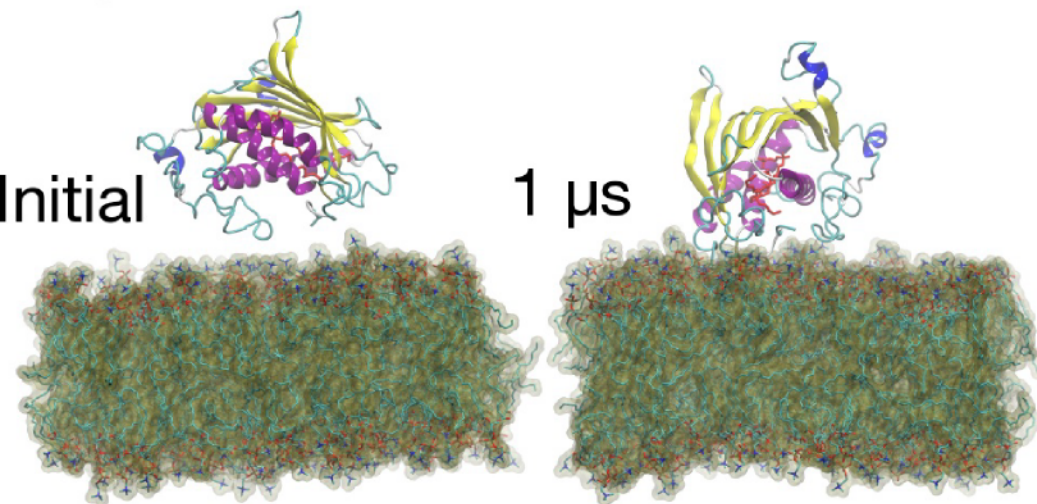
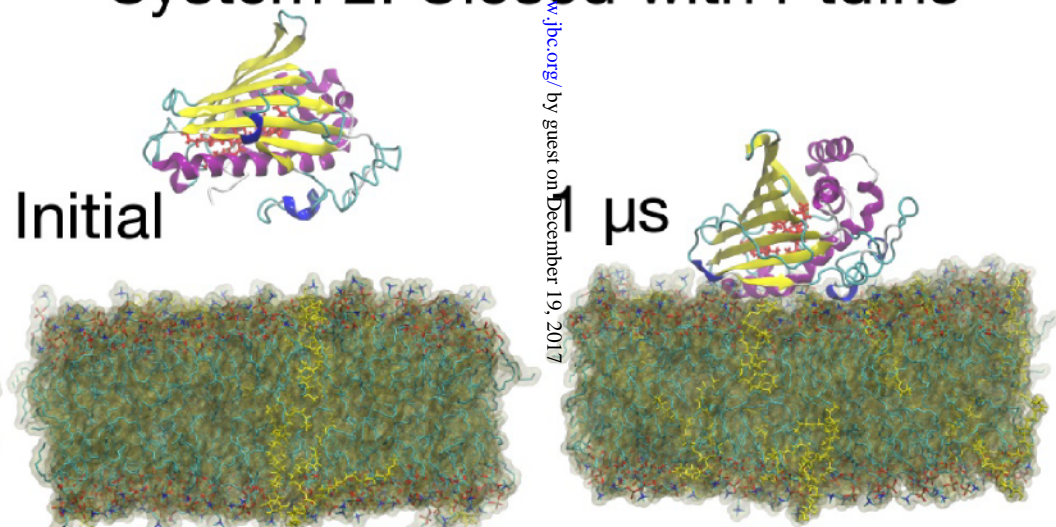


Figure 2

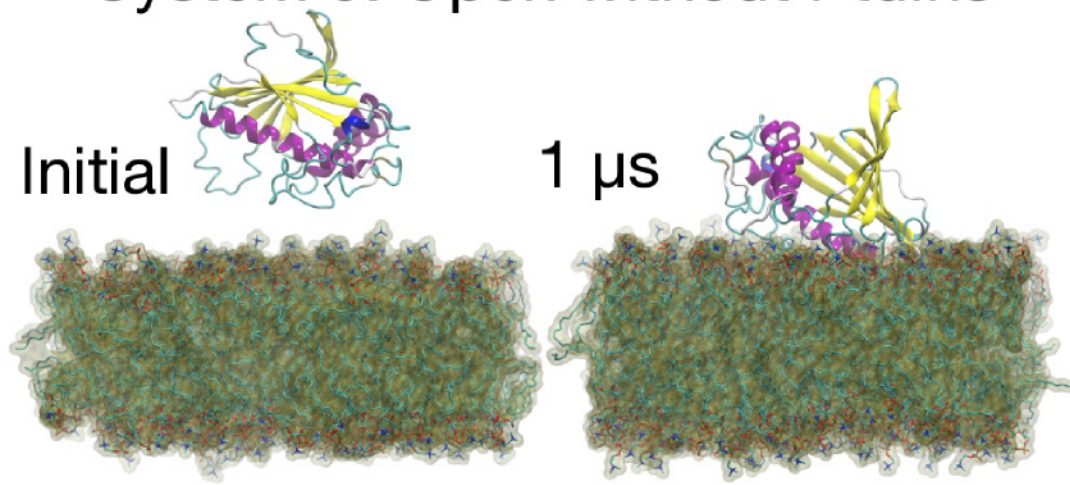
System 1: Closed without PtdIns



System 2: Closed with PtdIns



System 3: Open without PtdIns



System 4: Open with PtdIns

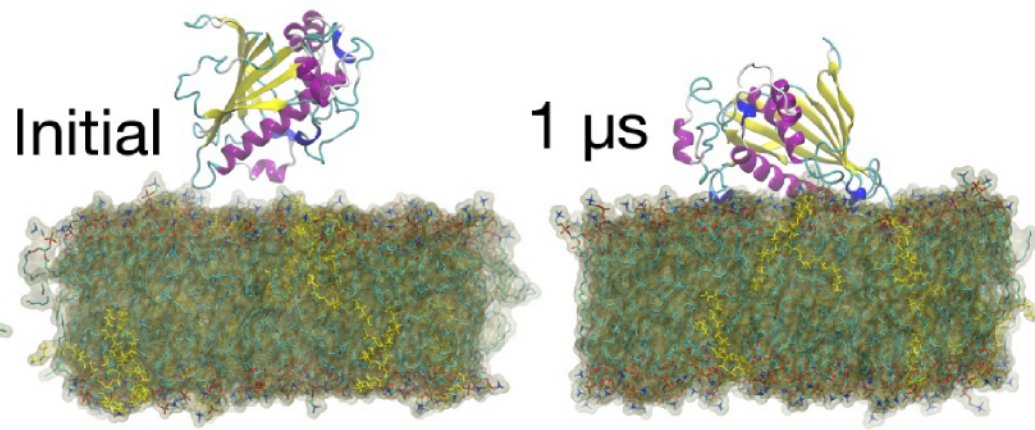
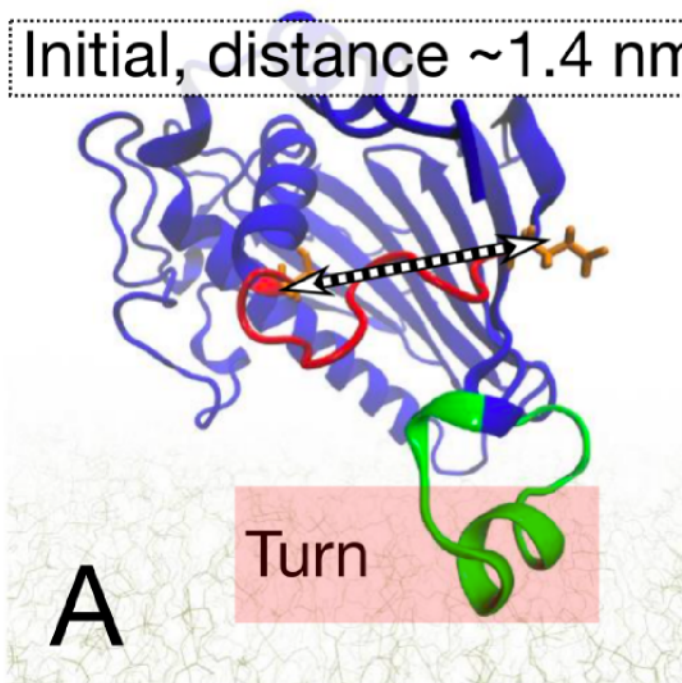


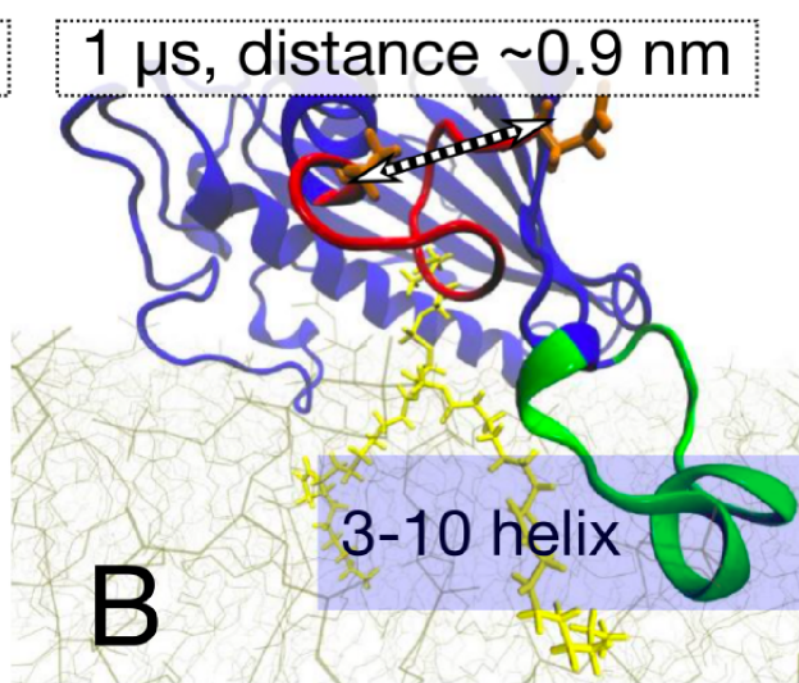
Figure 3

System 4: Open with PtdIns

Initial, distance ~ 1.4 nm



1 μ s, distance ~ 0.9 nm



1 μ s, lipid engaged, two presentations

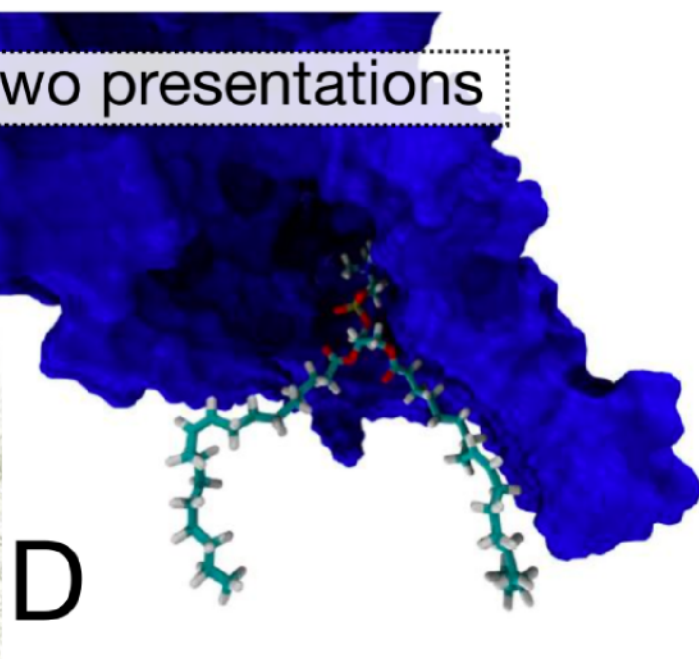
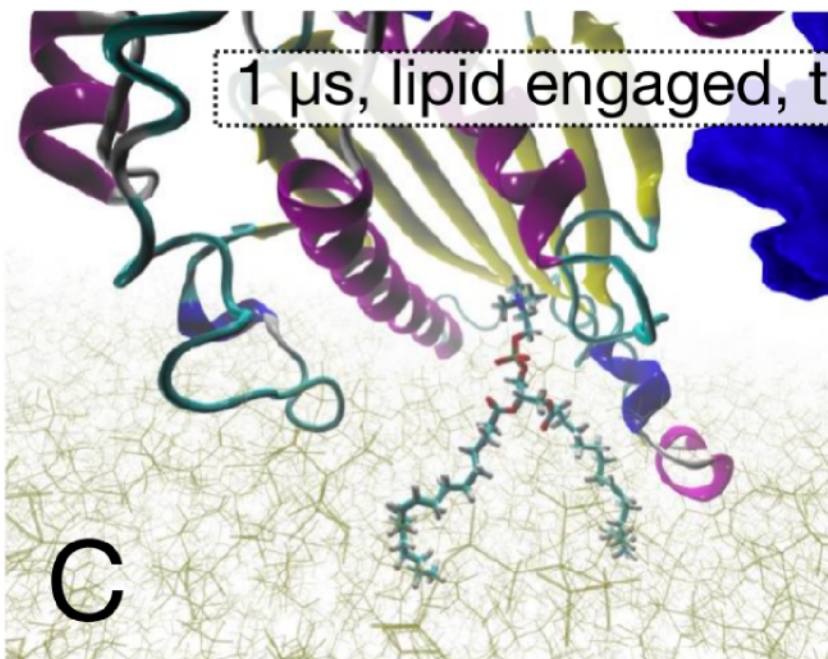


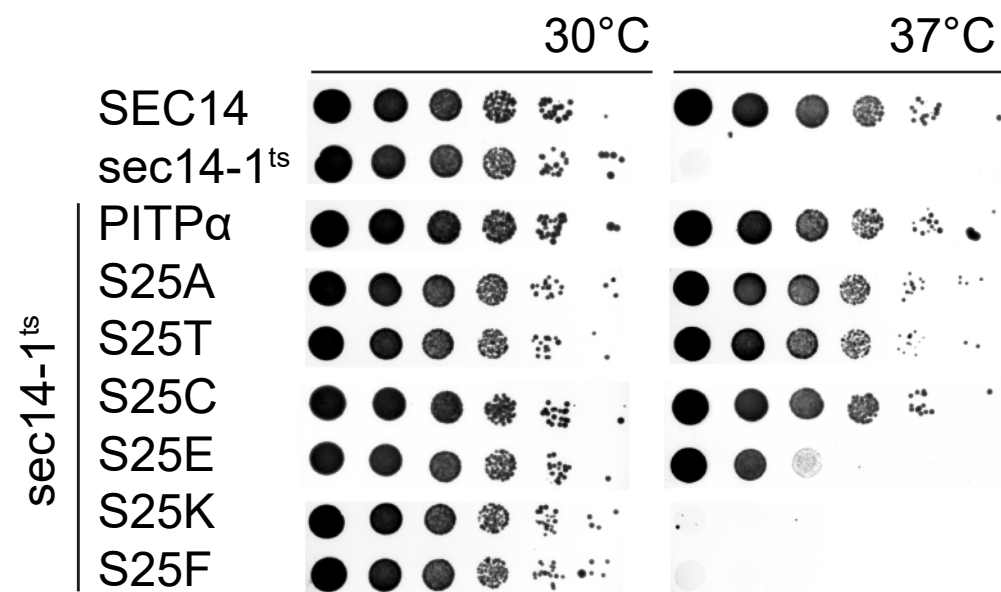
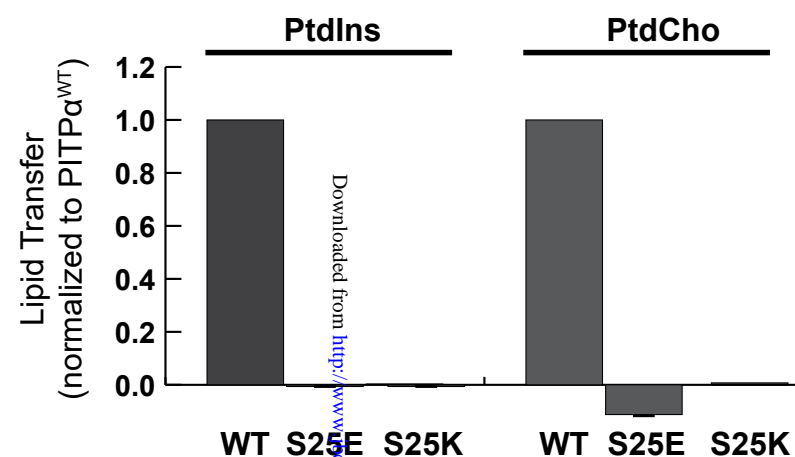
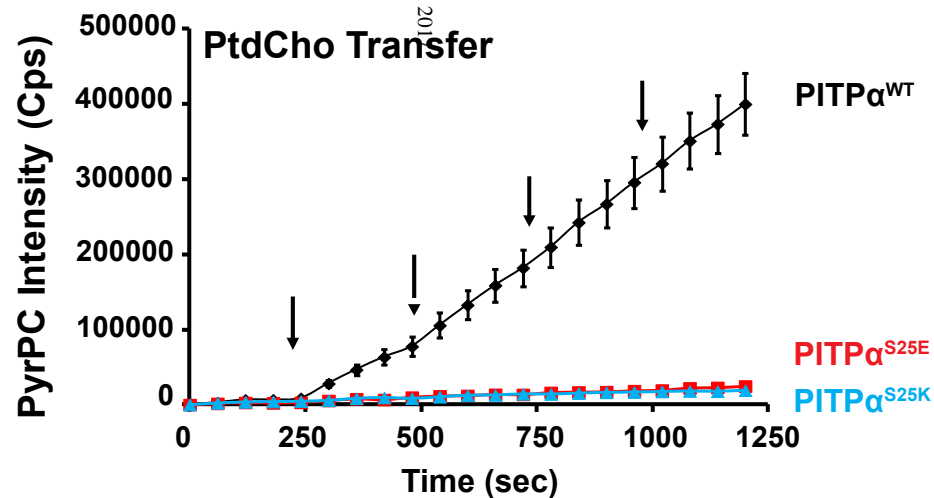
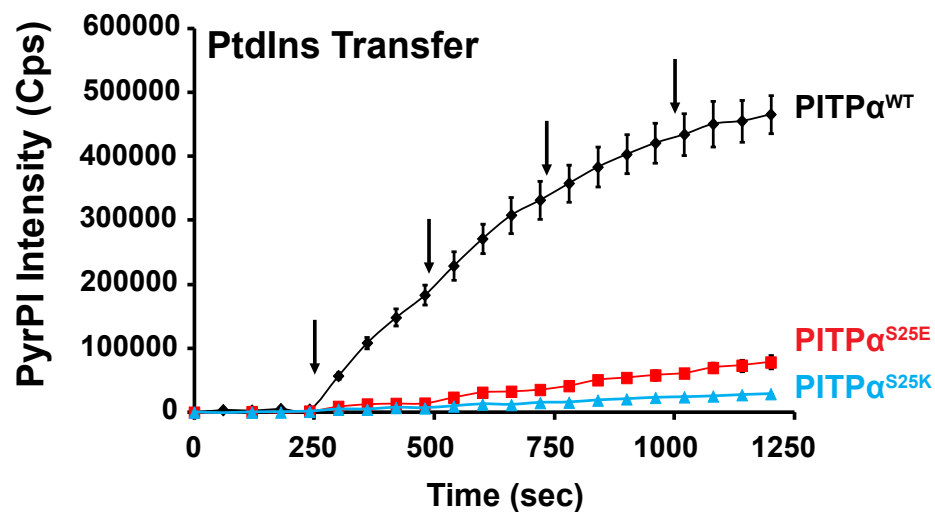
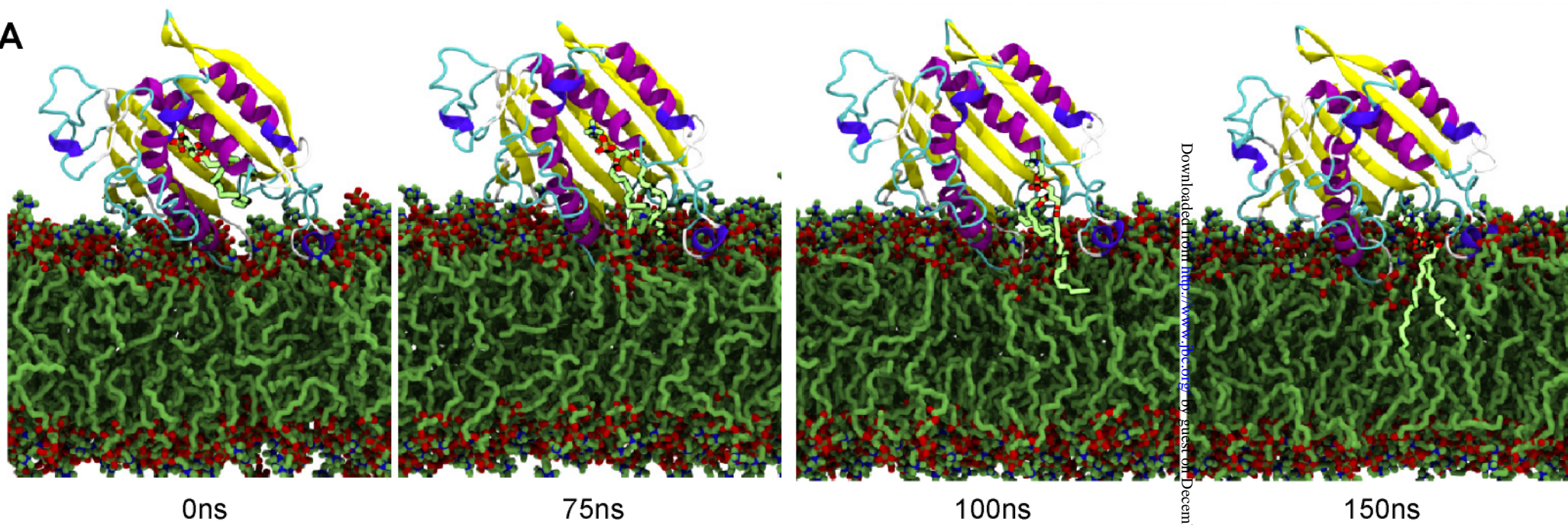
Figure 4**A****B****C**

Figure 5**A**

0ns

75ns

100ns

150ns

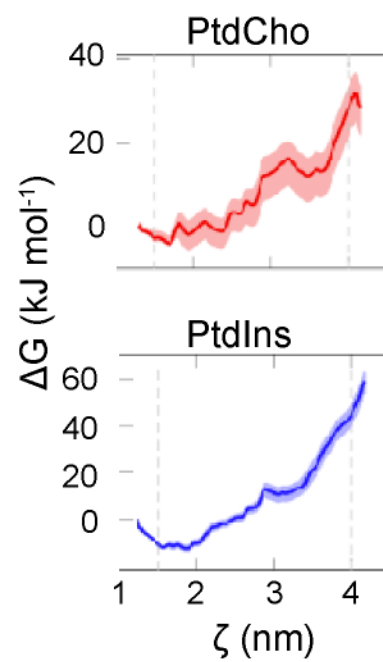
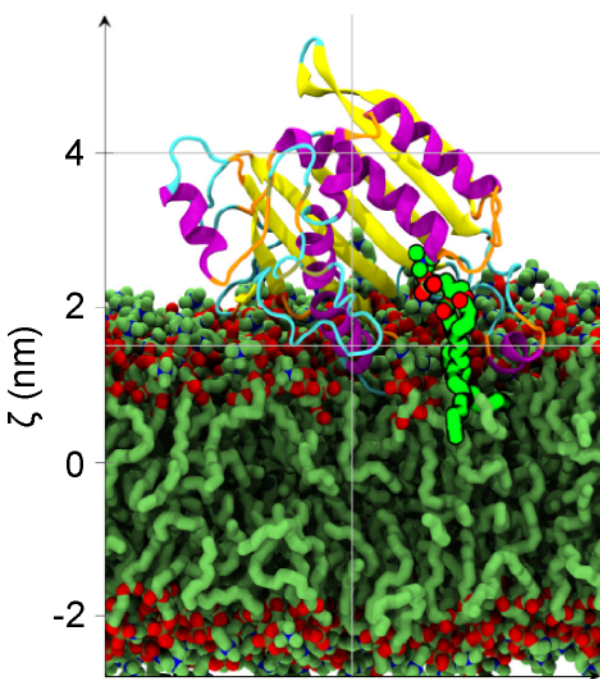
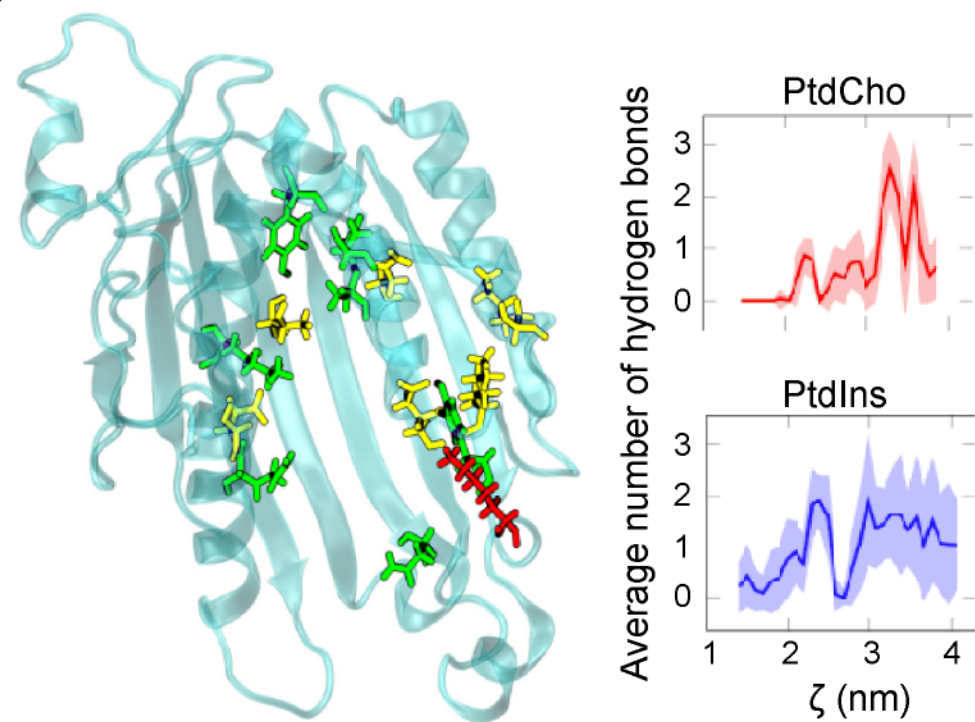
Downloaded from <http://www.rsc.org/> by guest on December 19, 2017**B****C**

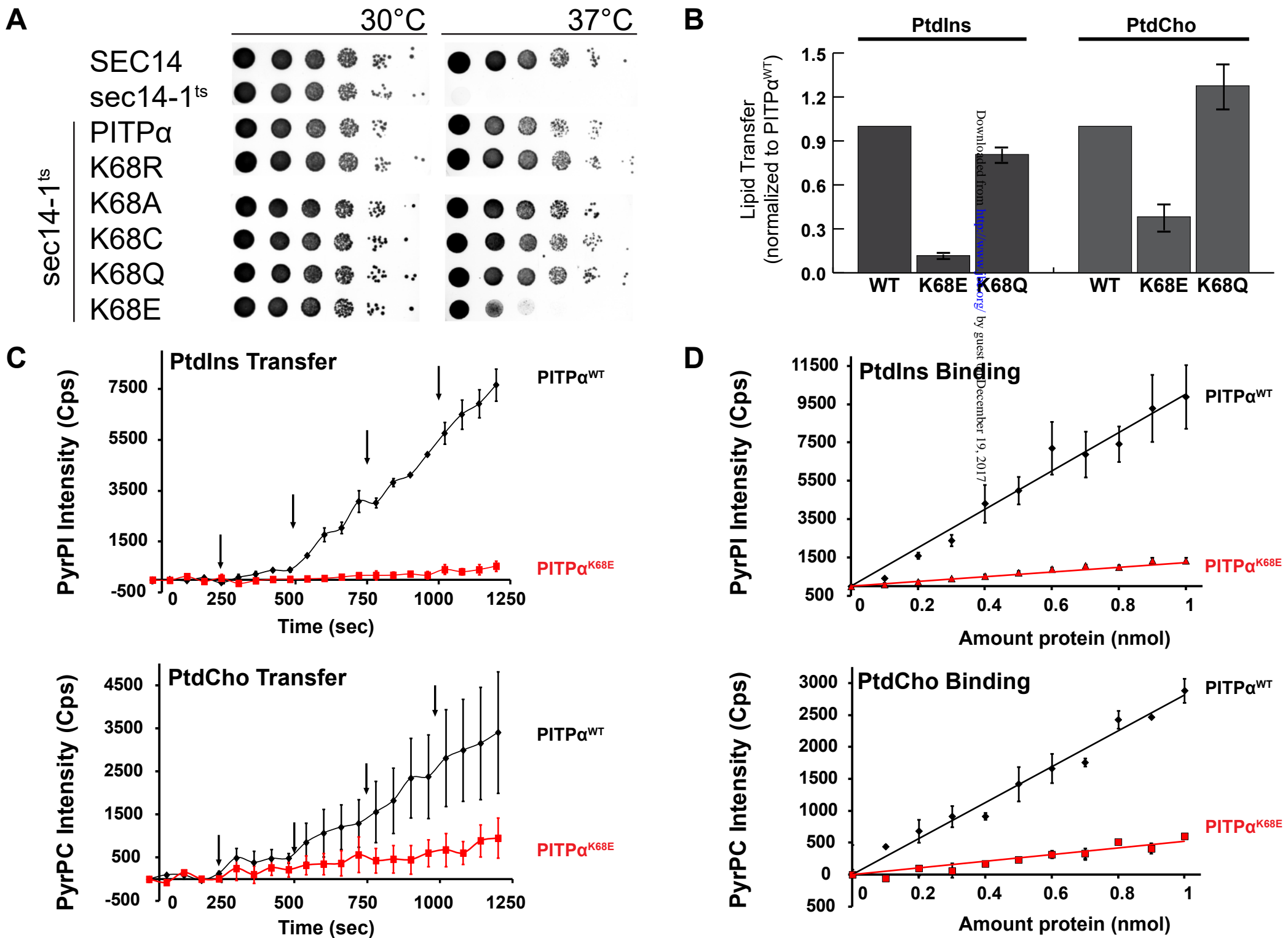
Figure 6

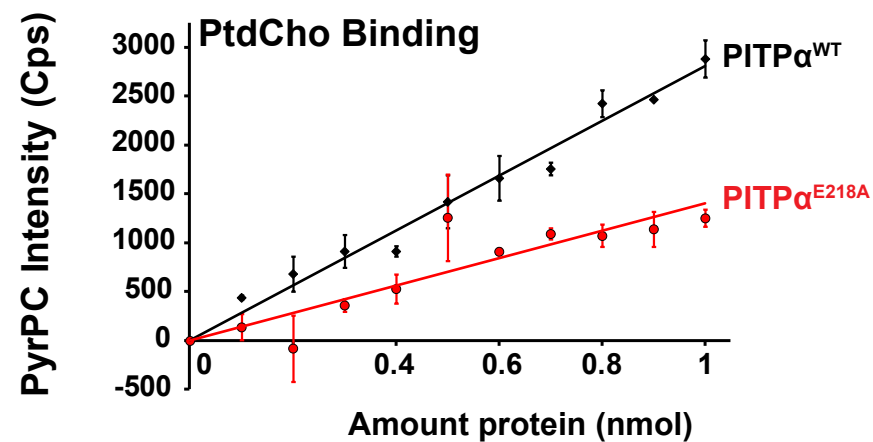
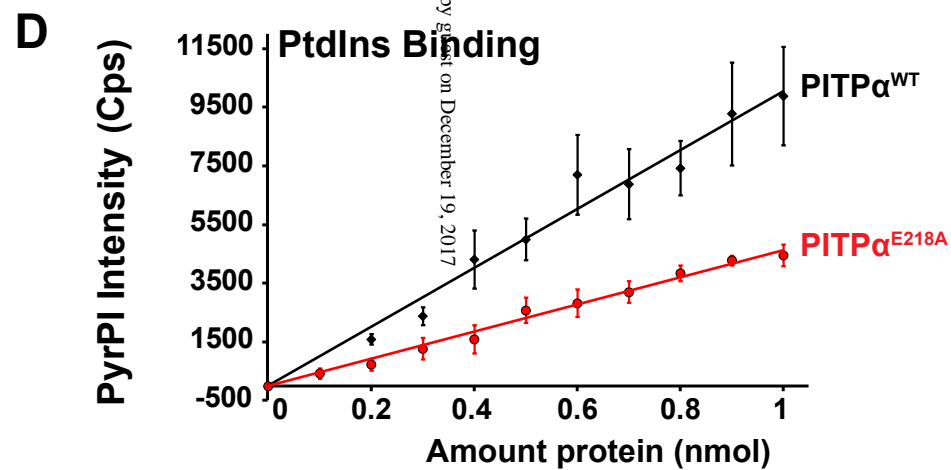
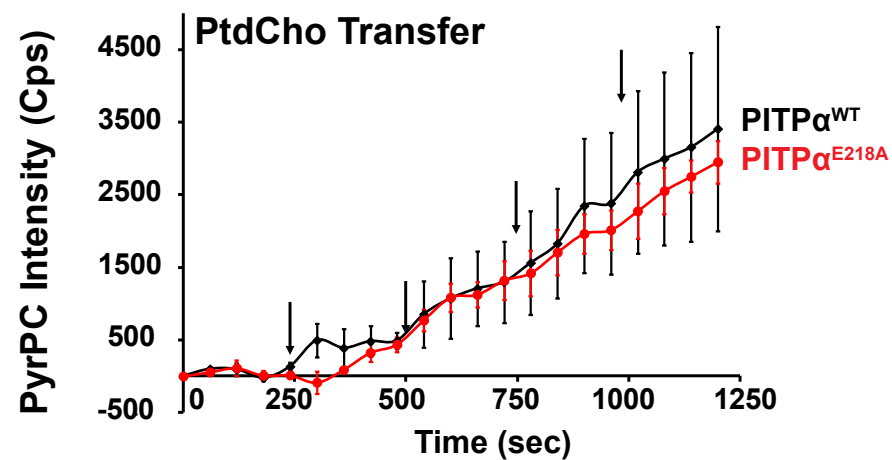
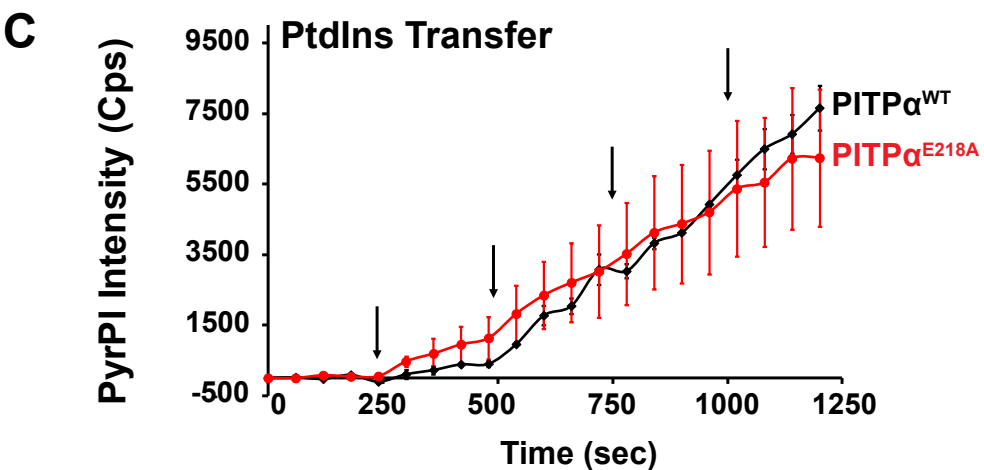
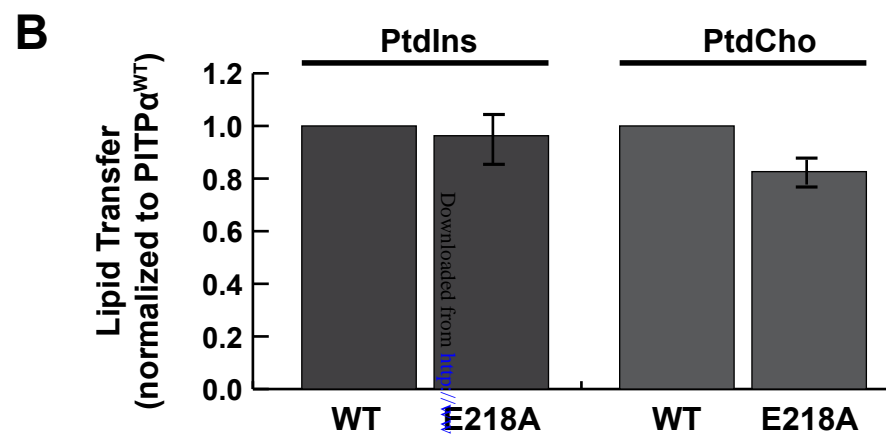
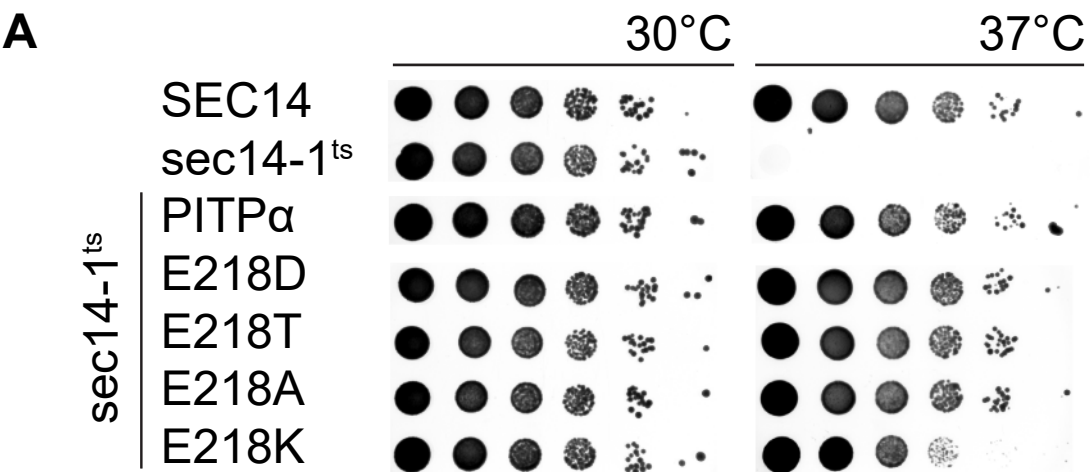
Figure 7

Figure 8

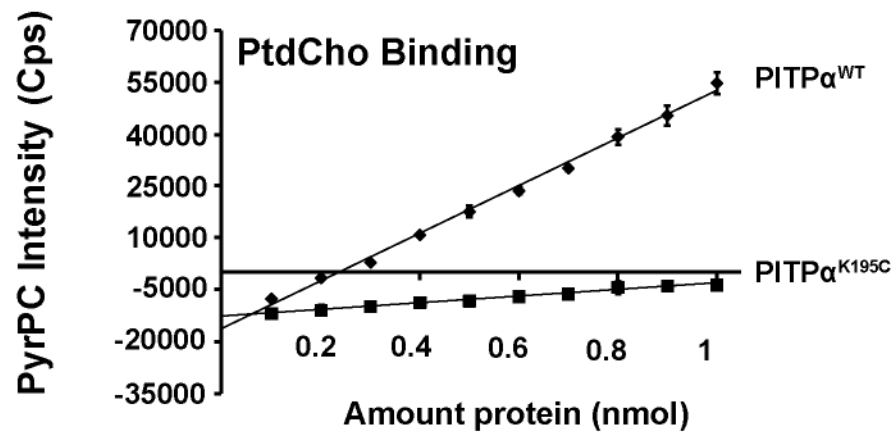
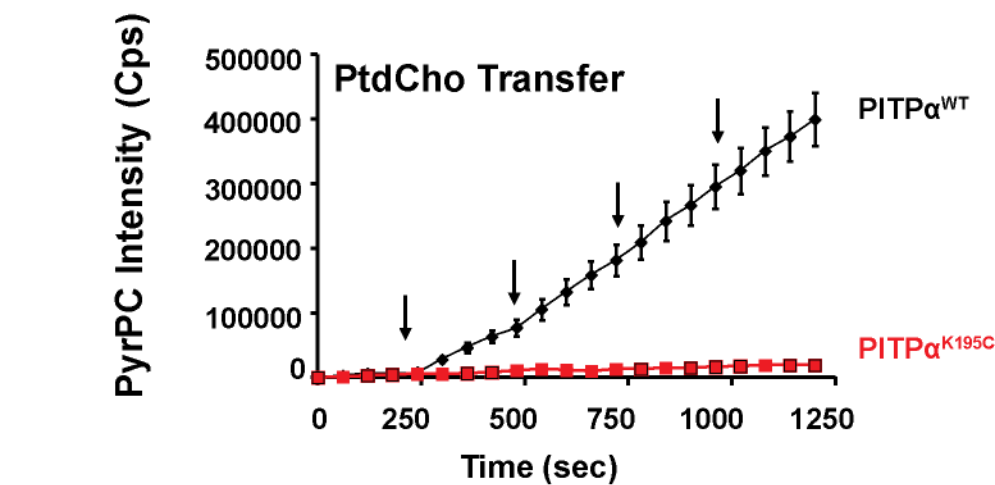
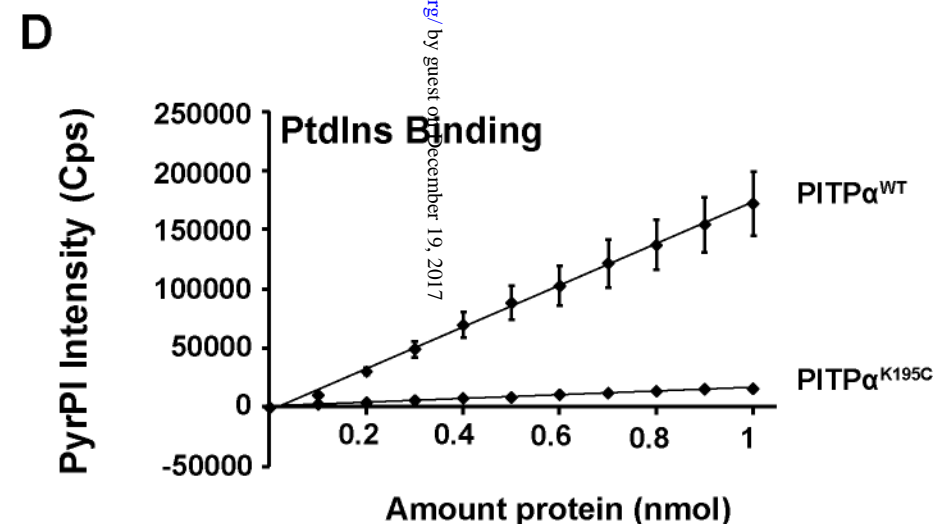
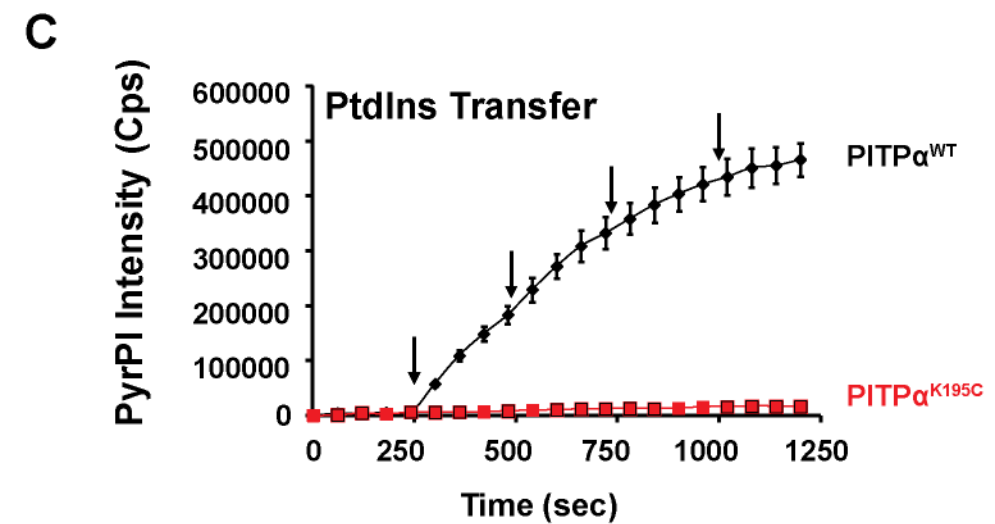
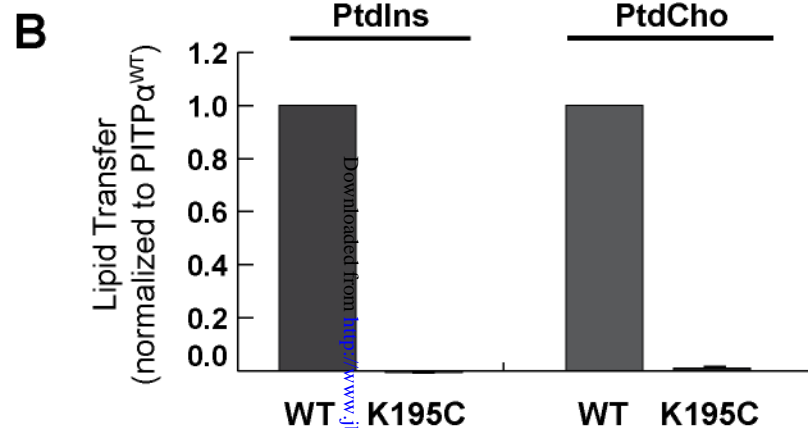
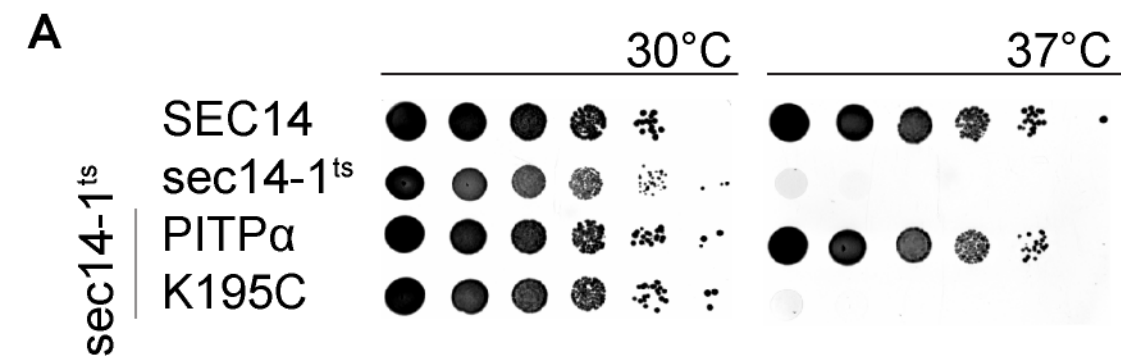
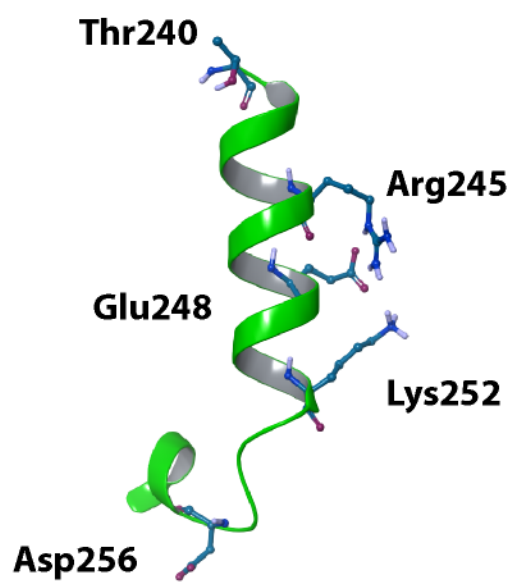
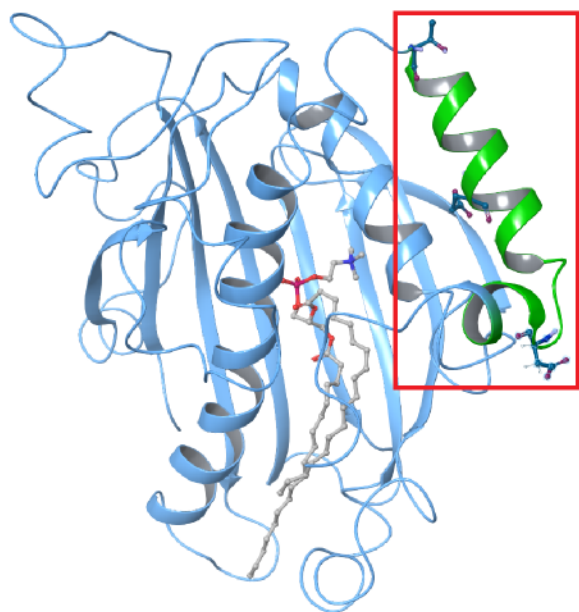
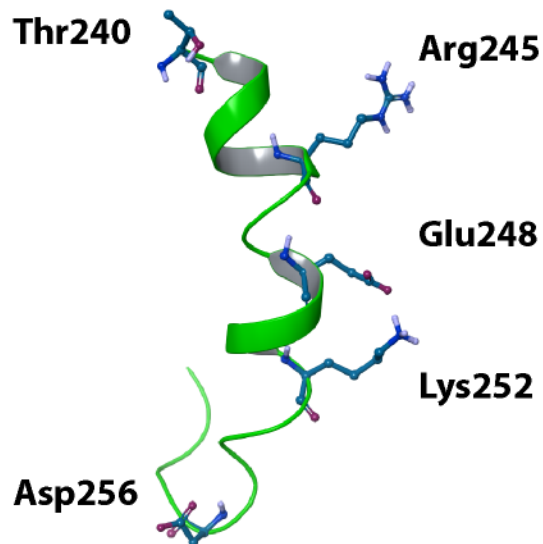
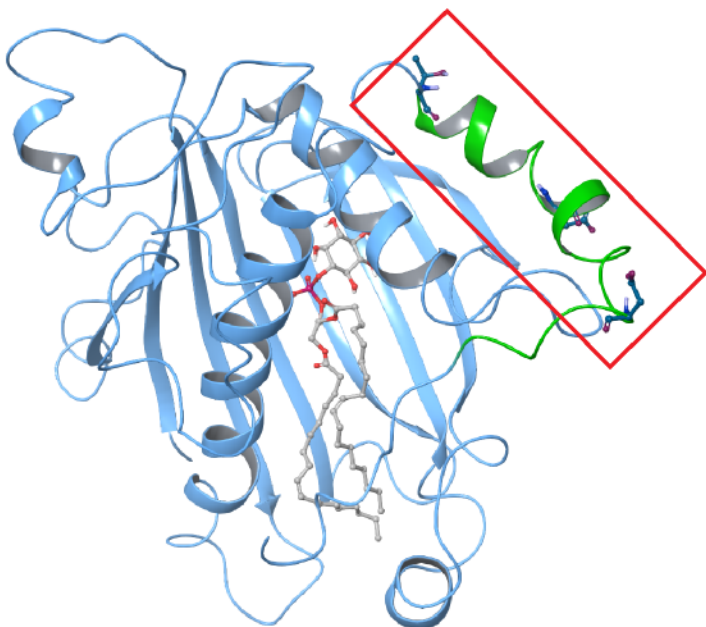


Figure 9

A



B



C

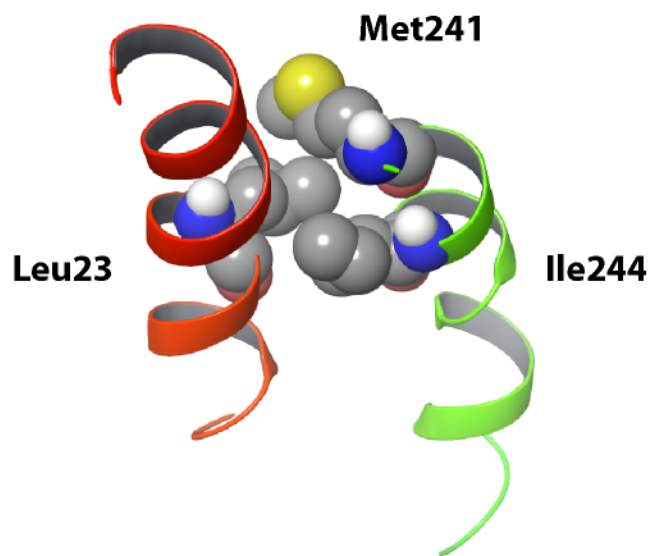
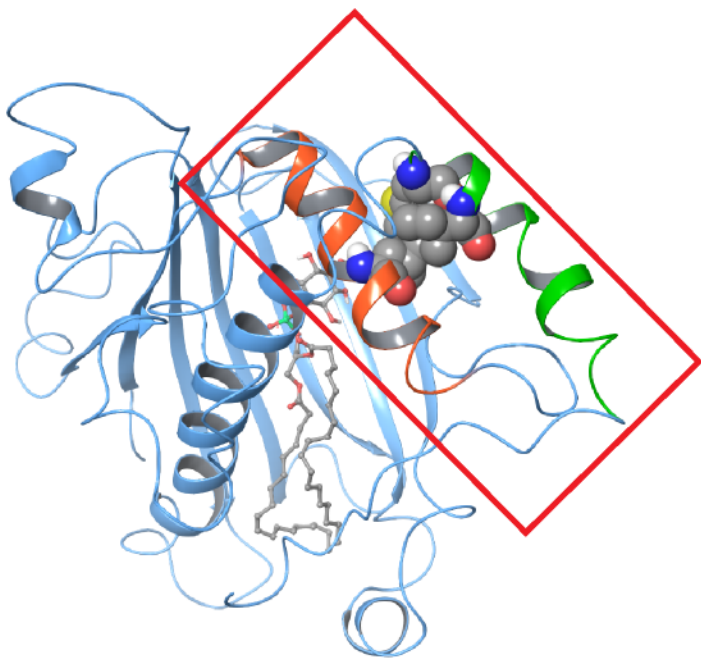


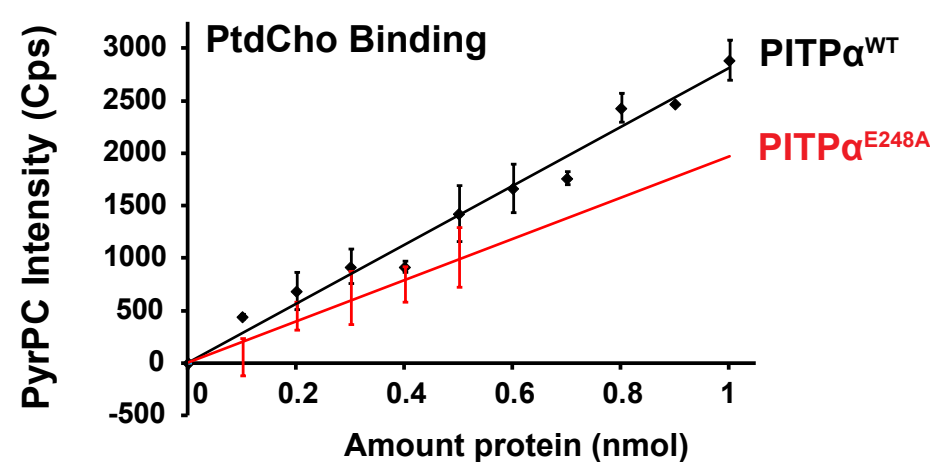
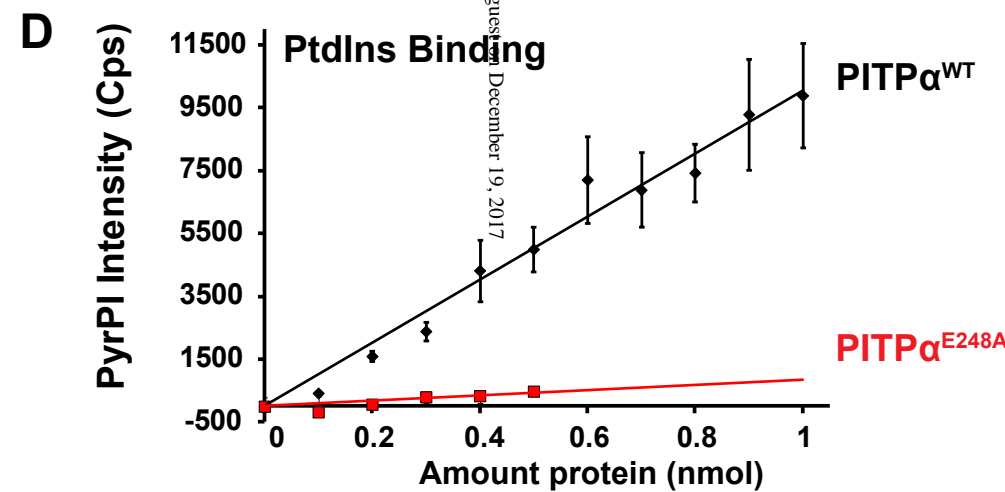
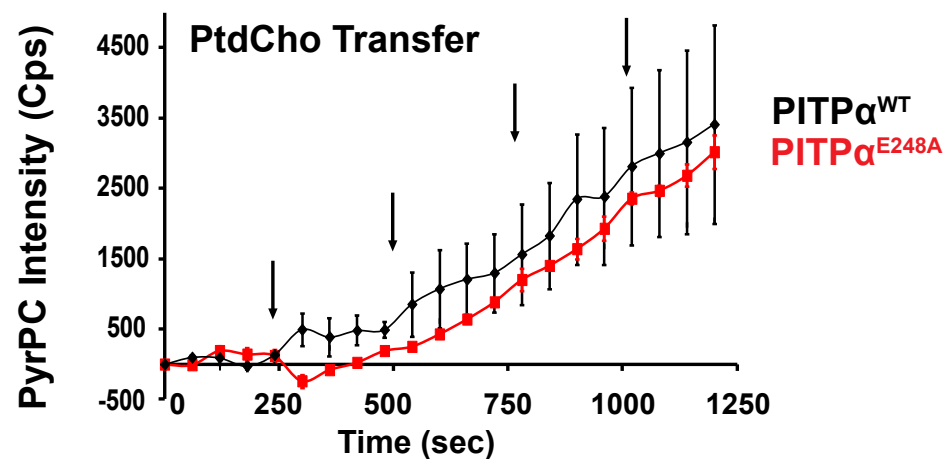
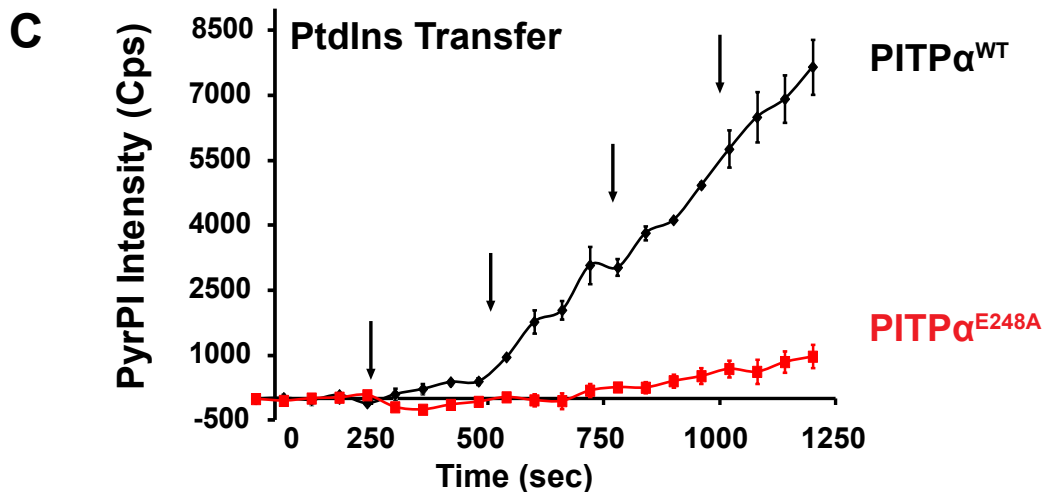
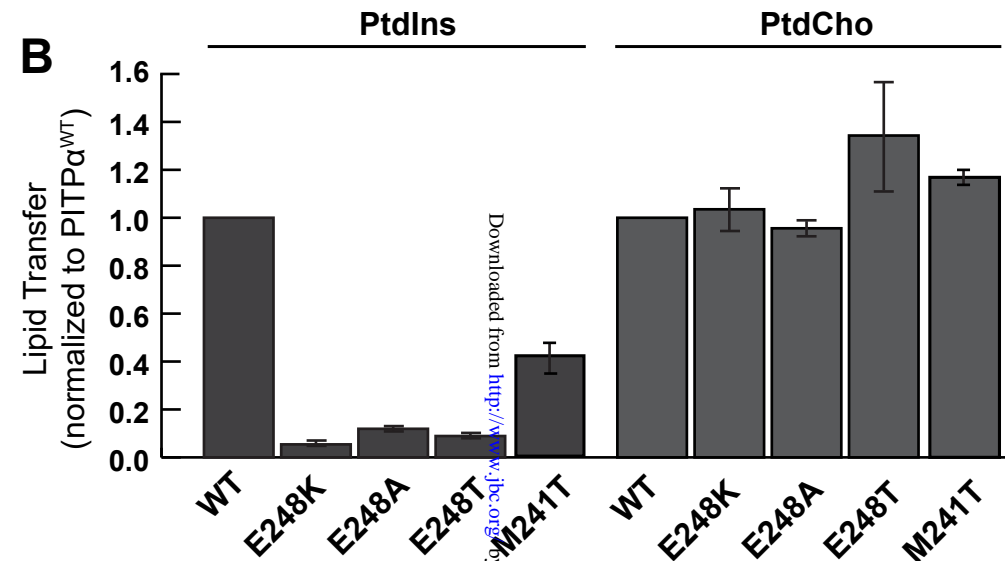
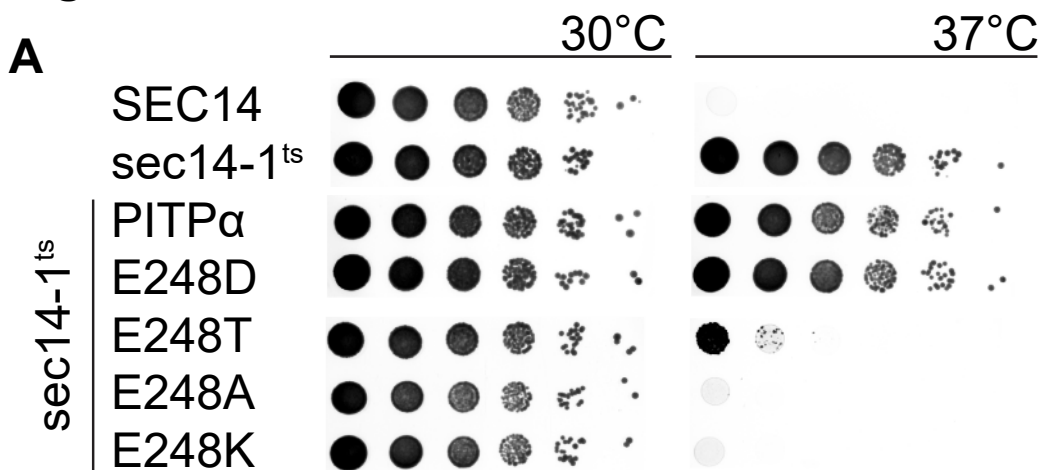
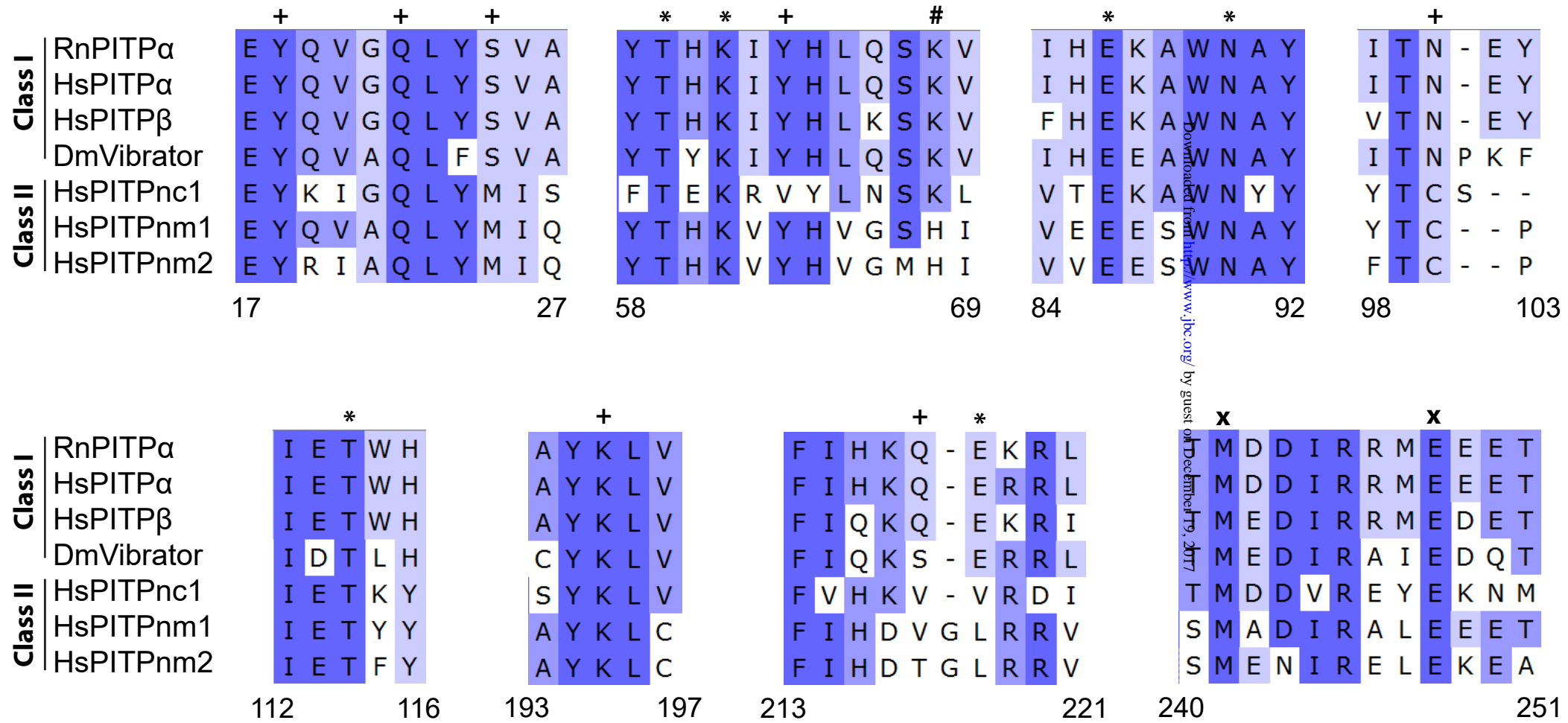
Figure 10

Figure 11



**Dynamics and Energetics of the Mammalian Phosphatidylinositol Transfer Protein
Phospholipid Exchange Cycle**

Aby Grabon, Adam Orłowski, Ashutosh Tripathi, Joni Vuorio, Matti Javanainen, Tomasz Róg, Max Lönnfors, Mark I. McDermott, Garland Siebert, Pentti Somerharju, Ilpo Vattulainen and Vytas A. Bankaitis

J. Biol. Chem. published online July 17, 2017

Access the most updated version of this article at doi: [10.1074/jbc.M117.791467](https://doi.org/10.1074/jbc.M117.791467)

Alerts:

- [When this article is cited](#)
- [When a correction for this article is posted](#)

[Click here](#) to choose from all of JBC's e-mail alerts

Supplemental material:

<http://www.jbc.org/content/suppl/2017/07/17/M117.791467.DC1>